NASA TECHNICAL NOTE

NASA TN D-6928

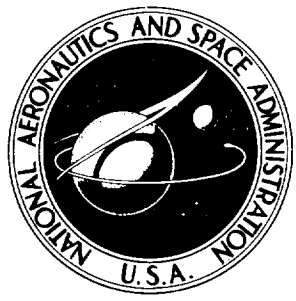

NASA TN D-6928

ANALYSIS OF AN ELECTROHYDRAULIC AIRCRAFT CONTROL-SURFACE SERVO AND COMPARISON WITH TEST RESULTS

by John W. Edwards

Flight Research Center
Edwards, Calif. 93523

NATIONAL AERONAUTICS AND SPACE ADMINISTRATION • WASHINGTON, D. C. • AUGUST 1972

1. Report No. NASA TN D-6928	2. Government Accession No.	3. Recipient's Catalog No.
4. Title and Subtitle ANALYSIS OF AN ELECTROHYDRAULIC AIRCRAFT CONTROL-SURFACE SERVO AND COMPARISON WITH TEST RESULTS		5. Report Date August 1972 6. Performing Organization Code
7. Author(s) John W. Edwards		8. Performing Organization Report No. H-629 10. Work Unit No. 136-62-02-00-24
9. Performing Organization Name and Address NASA Flight Research Center P. O. Box 273 Edwards, California 93523		11. Contract or Grant No. 13. Type of Report and Period Covered Technical Note
12. Sponsoring Agency Name and Address National Aeronautics and Space Administration Washington, D. C. 20546		14. Sponsoring Agency Code
15. Supplementary Notes		

16. Abstract

An analysis of an electrohydraulic aircraft control-surface system is made in which the system is modeled as a lumped, two-mass, spring-coupled system controlled by a servo valve. Both linear and nonlinear models are developed, and the effects of hinge-moment loading are included. Transfer functions of the system and approximate literal factors of the transfer functions for several cases are presented. The damping action of dynamic pressure feedback is analyzed. Comparisons of the model responses with results from tests made on a highly resonant rudder control-surface servo indicate the adequacy of the model. The effects of variations in hinge-moment loading are illustrated.

17. Key Words (Suggested by Author(s))	18. Distribution Statement
Hydraulic control systems Aircraft hydraulic systems Control systems	Unclassified - Unlimited

19. Security Classif. (of this report)	20. Security Classif. (of this page)	21. No. of Pages	22. Price*
Unclassified	Unclassified	72	$3.00

* For sale by the National Technical Information Service, Springfield, Virginia 22151

ANALYSIS OF AN ELECTROHYDRAULIC AIRCRAFT CONTROL-SURFACE SERVO AND COMPARISON WITH TEST RESULTS

John W. Edwards
Flight Research Center

INTRODUCTION

During the past decade, the use of electrohydraulic servomechanisms in aircraft flight-control systems has become commonplace. They are used to provide power boost, stability augmentation control inputs, or primary control of the vehicle. Because of weight and space limitations, there is always a design trade-off in the installation of such a system concerning the structural stiffness of its components. In a well-designed electrohydraulic control-surface system, a well-behaved system with a first-order-lag dynamic response may be achieved. The system time constant is determined by the position feedback gain.

In some instances this desirable response is not achieved because excessive structural compliance causes the system to be highly resonant. This was true of a rudder control servo installed in the NASA general purpose airborne simulator (GPAS). Attempts to damp such systems have led to the use of dynamic pressure feedback (DPF), in which high-passed pressure feedback provides the necessary damping.

The literature on electrohydraulic systems is extensive (refs. 1 to 8, for example); however, there does not seem to be any readily available analysis of this type of system, which is often encountered in aircraft control-surface systems. The purpose of this report is to analyze a lumped, two-mass model of an aircraft control-surface servo and to illustrate the use of DPF. The effect of hinge-moment loading of the control surface is included. The model is linearized, transfer functions of the pertinent variables are derived, and the effectiveness of DPF in damping the load resonance is investigated. The nonlinear and linear responses of the model are compared with experimental measurements of the highly resonant rudder control servo installed in the GPAS.

SYMBOLS

A	piston area, in^2
B	general coefficient matrix
B_c	coulomb friction coefficient, lb
B_v	viscous friction coefficient, $lb/ft\text{-}sec^{-1}$

C_h	control-surface hinge-moment coefficient
$C_{h_\delta}, C_{h_\theta}$	coefficients in hinge-moment equation
$\bar{c}$	control-surface reference chord, ft
e	servovalve command voltage, V
F	general coefficient matrix
f	frequency, Hz
G, G_1, G_2	feedback gain matrices
H_s	control-surface hinge moment, ft-lb
I	control-surface moment of inertia, slug-ft^2
$j = \sqrt{-1}$	
K	spring constant, ft-lb/rad
K_c	servovalve flow-pressure gain, in^3-sec^{-1}/psi
K_p	pressure feedback gain, V/psi
K_q	servovalve flow gain, in^3-sec^{-1}/in.
K_s	servovalve first-stage gain, in/V
K_v	servovalve proportionality constant, in^3-sec^{-1}/in$\sqrt{\text{psi}}$
K_x	position feedback gain, V/ft
K_1, K_2	coefficients in hinge-moment equation, ft-lb/rad
K_β	gain constant of $\frac{\delta_r}{\beta}(s)$ transfer function
L	servovalve coil inductance, H
L_g	scale length of turbulence, ft
l	moment arm, ft
m_p	piston mass, slugs
P_F	output of high-pass filter, psi
P_L	differential load pressure, psid

P_s	hydraulic source pressure, psi
P_1, P_2	actuator chamber pressures, psi
p_1, p_2, p_3	real poles of transfer functions
Q_L	hydraulic fluid flow rate, in^3/sec
Q_1, Q_2, Q_3, Q_4	hydraulic fluid flows in servovalve, in^3/sec
R	servovalve coil resistance, ohms
S	control-surface reference area, ft^2
s	Laplace transform variable
$\underline{u}$	control input vector
V	volume of fluid between servovalve and actuator, in^3
V_a	aircraft velocity, ft/sec
v_g	lateral gust velocity, ft/sec
$\underline{x}$	state vector
x_p	piston displacement, ft
x_s	servovalve spool displacement, in.
x_1	auxiliary variable introduced in model
z_1	real zero of transfer function
β	aircraft angle of sideslip, rad or deg
β_e	bulk modulus of elasticity of hydraulic fluid, psi
$\Delta(s), \Delta_1$	denominator of transfer function
δ	control-surface deflection, rad
δ_r	rudder deflection, rad or deg
$\zeta_c, \zeta_t, \zeta_2, \zeta_p$	damping ratios
θ	angle of incidence at control surface, rad
ρ	atmospheric density, $slugs/ft^3$

σ	real part of complex number
σ_g	root-mean-square value of v_g, ft/sec
τ_p	time constant of high-pass filter, sec
τ_s	time constant of first stage of servovalve, sec
$\Phi_{v_g}(\omega)$	power spectrum of lateral gust
ω	frequency, rad/sec
$\omega_s, \omega_c, \omega_h, \omega_p, \omega_t, \omega_2$	open-loop natural frequencies, rad/sec

Subscripts:

c	command signal
g	gust
h	mode caused by hinge-moment loading
max	maximum operating value
ss	steady state

A single dot over a quantity indicates the first derivative with respect to time; double dots indicate the second derivative with respect to time.

DEVELOPMENT OF MODEL

The system analyzed in this report is an aircraft control-surface control system powered by an electrohydraulic servovalve (figs. 1(a) to 1(c)). The system is similar to the stability augmenters or power boost units in many existing systems. The mechanical linkages to a pilot's controller are not shown in figure 1(a) because only the electrohydraulic control system is analyzed.

The command voltage to the servo system may be derived from the measurement of rate or attitude gyros or from the pilot's controller position. The electrical input to the servovalve results in hydraulic fluid flow to one side of the actuator or the other and causes piston and control-surface motion. To make the system stable, a measurement of the piston position is fed back and summed with the command voltage. In some systems, this position loop closure results in lightly damped oscillations. If this occurs, it has been found to be advantageous to provide an additional feedback signal, that of the hydraulic differential pressure, across the piston. When this second feedback signal is properly conditioned, a well-damped system usually results.

Both the position and pressure measurements are shown as if they were made with electrical transducers. This is only for ease of illustration. Systems are in use

which provide these feedbacks mechanically. Both methods of feedback, however, result in similar system responses.

Figure 1(b) shows the mechanical components of the control-surface control system, a two-mass, spring-coupled system. The load moment of inertia is I and the mass of the actuator piston is m_p. The piston is driven by hydraulic pressure, P_L, which acts on the piston head area, A, and applies torque to the load through a moment arm, l. The linear piston position is shown as x_p, and the angular surface position is indicated by δ. There is viscous friction, B_v, and coulomb friction, B_c, between the piston and the cylinder. The surface hinge moment is shown as H_s. It is assumed that the compliance in the system is in the torque tube where the piston is attached, giving the rotary spring constant, K. For convenience, structural damping of the load is not considered, because structural damping ratios are characteristically small.

Systems of the type shown in figure 1 are discussed in references 1 to 5. Reference 1 derives pertinent transfer functions for a simplified model (m_p is assumed to be zero and no actuator friction is included). References 2 and 3 describe a similar system in a spacecraft engine servo and illustrate nonlinear techniques for studying possible limit cycles. Reference 4 describes the aileron actuation system used on a B-52 airplane and mentions high-frequency control-valve-generated noise (audible noise termed "honk"), an effect which will be discussed later. This report is a summary of many of the practical problems which may be encountered in a hydraulic system. Reference 5 analyzes the various configurations of aircraft hydraulic systems in detail.

Electrohydraulic Servovalve

A critically centered threeland, four-way, two-stage servovalve is assumed to be the power control device for the hydraulic system analyzed. The servovalve consists of a first-stage electrical torque motor, which controls pressure on the ends of the spool (the second stage, fig. 1(c)). The actuator used in this analysis is assumed to be double-ended; that is, both sides of the piston head have equal areas. Movement of the spool opens orifices connected to a pressure supply and sink and to both sides of the main actuator piston. The input to the servovalve is an electrical current, or voltage, and the output is the differential load pressure developed across the piston. An intermediate variable is the spool position, x_s. Servovalve dynamics are analyzed in references 1, 6, 7, and 8. The succeeding development follows that in reference 6.

To develop a model of the servovalve, the relationship of the spool position, x_s, to the load pressure, P_L, must be known. It may be obtained by applying the orifice flow equation (ref. 6, p. 41) to each of the four orifices shown in figure 1(c). The hydraulic fluid flows through these orifices are labeled Q_1 through Q_4. The load flow, Q_L, satisfies the relations

$$Q_L = Q_1 - Q_4$$

$$Q_L = Q_3 - Q_2$$

The orifice flow equation shows the relationship between the fluid flow through an orifice, the orifice opening, and the pressure drop across the orifice. In the development of the orifice equation, it was assumed that the flow through the orifice was incompressible. Applying the orifice equation to each of the four orifices and using the relations given for Q_L and P_L,

$$Q_L = K_v x_s \sqrt{P_s - \frac{x_s}{|x_s|} P_L} \tag{1}$$

where K_v is a proportionality constant. Later in this report the effect of fluid compressibility in the actuator chamber is added to the model. This does not invalidate the use of the orifice flow equation here, however, because it is applied only to flows in the immediate vicinity of the orifice (within 1 orifice diameter of the orifice) where the assumption of incompressibility is valid.

Equation (1) may be expanded in a Taylor's series about a nominal operating condition, giving to first order the equation

$$\Delta Q_L = K_q \Delta x_s - K_c \Delta P_L \tag{2}$$

where Δ indicates a deviation from the nominal and

$$K_q = \frac{\partial Q_L}{\partial x_s} = K_v \sqrt{P_s - \frac{x_s}{|x_s|} P_L} \tag{3a}$$

$$K_c = -\frac{\partial Q_L}{\partial P_L} = \frac{1}{2} \frac{K_v |x_s|}{\sqrt{P_s - \frac{x_s}{|x_s|} P_L}} \tag{3b}$$

Common nominal operating conditions are $P_L = 0$ and $x_s = x_{s_{max}}$, giving

$$K_q = K_v \sqrt{P_s} \tag{4a}$$

$$K_c = \frac{1}{2} \frac{K_v x_{s_{max}}}{\sqrt{P_s}} \tag{4b}$$

The quantity K_q is the valve flow gain and is important in determining the servo position loop gain. The quantity K_c is the valve flow-pressure gain. Equations (3a) and

(3b) are nonlinear equations for the coefficients of equation (2), whereas equations (4a) and (4b) provide linear approximations to the coefficients. An expression of intermediate accuracy can be obtained by expanding the square root in equation (1) as

$$Q_L = K_v x_s P_s^{\frac{1}{2}} \sqrt{1 - \frac{x_s}{|x_s|}\frac{P_L}{P_s}} \cong K_v x_s \left(P_s^{\frac{1}{2}} - \frac{1}{2}\frac{x_s}{|x_s|}\sqrt{\frac{P_L}{P_s}} \right)$$

If K_q and K_c are determined from this expression and the same nominal operating condition is used,

$$K_q = K_v \sqrt{P_s} \tag{5a}$$

$$K_c = \frac{1}{2}\sqrt{\frac{K_v |x_s|}{P_s}} \tag{5b}$$

Equations (5a) and (5b) are used later in an analog simulation of the model, and equations (4a) and (4b) are used for linear analytical calculations. Henceforth, the Δ terms will be omitted from equation (2), giving

$$Q_L = K_q x_s - K_c P_L \tag{6}$$

Aircraft hydraulic systems commonly utilize a 3000-psi source pressure. The load pressures encountered are usually much lower than this source pressure. In this instance the differences of equations (3a) and (3b), (4a) and (4b), and (5a) and (5b) are small, and the use of the linear equations is justified.

The continuity equation is used to relate the flow through the servovalve to the mechanical motion of the system. Mass flow through the servovalve, given by equation (6), is equated to flow to the actuator. The flow to the actuator is the sum of piston displacement and flow due to fluid compressibility (ref. 6):

$$Q_L = \frac{V}{4\beta_e}\dot{P}_L + 12A\dot{x}_p \tag{7}$$

where x_p is piston displacement, V is the total volume between the servovalve and piston, and β_e is the bulk modulus of elasticity of the hydraulic fluid. The numeral 12 occurs because valve coefficients are expressed in terms of cubic inches per unit. Equating equation (6) to equation (7),

$$\frac{V}{4\beta_e}\dot{P}_L + 12A\dot{x}_p = K_q x_s - K_c P_L$$

$$\dot{P}_L = \frac{4\beta_e}{V}(-K_c P_L - 12A\dot{x}_p + K_q x_s) \tag{8}$$

It is common to include the effects of leakage across the piston head and leakage to drain in equation (7), giving rise to leakage coefficients in equation (8). These terms are proportional to P_L, so K_c may be interpreted as a composite coefficient. Leakage is not considered explicitly in this report.

In equation (8), care must be taken to insure that all units are correct. It is assumed that the valve coefficients are given in cubic inches per unit, P_L and β_e in pounds per square inch, V in cubic inches, and x_p in feet.

The first-stage valve dynamics relating input voltage to spool displacement are also required for the model. The torque motor coils form a resistance-inductance (RL) electrical circuit which, when driven by a voltage source, exhibits a first-order-lag characteristic with time constant L/R and gain 1/R. The torque motor is loaded by the first-stage hydraulic flow and the spool. Analysis of this system is complicated (ref. 6). Fortunately, the response of the servovalve is extremely fast and can be modeled adequately for low-frequency approximation as a first-order lag (ref. 8). The time constant, τ_s, is approximated from manufacturer's test data as the 45° phase shift frequency of the valve frequency response.

The response of the valve is then given by

$$x_s(s) = \frac{K_s}{1 + \tau_s s} e(s) \tag{9}$$

where e(s) is the Laplace transformed voltage input.

The first stage of the servovalve exhibits several nonlinearities which may be important to the system response. The magnetic circuit of the torque motor coils will have some hysteresis. The magnitude of the hysteresis is given by manufacturer's test data as a percentage of maximum input current. Because the size of the hysteresis loop shrinks as the input signal amplitude decreases, this effect is usually not critical and will not be considered. Another nonlinearity is the friction between the spool and its housing, which gives rise to backlash in the output of the first stage of the servovalve. Thus there will be a threshold value of input current below which no change in valve output is noted. In well-designed valves, backlash can also be ignored.

Piston and Load Dynamics

The equations of the piston and load dynamics are also necessary for the model. From figure 1(b), the equation of motion of the piston mass is

$$m_p \ddot{x}_p = -\frac{K}{l}\left(\frac{x_p}{l} - \delta\right) - B_v \dot{x}_p + F_c + AP_L \tag{10}$$

where A is the piston area. The equation of motion of the control surface is

$$I\ddot{\delta} = -K\left(\delta - \frac{x_p}{l}\right) + H_s \tag{11}$$

The coulomb friction is given by $F_c = -B_c \frac{\dot{x}_p}{|\dot{x}_p|}$. The aerodynamic hinge moment, H_s, may be approximated as

$$H_s = \frac{1}{2}\rho V_a^2 S\bar{c}C_h \quad \text{(ref. 9)}$$

where

$$C_h = C_{h_\theta}\theta + C_{h_\delta}\delta$$

and θ indicates the angle of incidence of the control surface. Thus

$$H_s = K_1\theta - K_2\delta \tag{12}$$

where

$$K_1 = \frac{1}{2}\rho V_a^2 S\bar{c}C_{h_\theta}$$

$$K_2 = -\frac{1}{2}\rho V_a^2 S\bar{c}C_{h_\delta}$$

Control Law

To complete the model the control law must be specified. It is assumed that there will be position feedback and high-passed pressure feedback plus a command input to form the voltage signal, e. The pressure feedback is modeled as

$$P_F(s) = \frac{\tau_p s}{1 + \tau_p s} P_L(s) \tag{13}$$

where P_F indicates a filtered pressure signal. It is assumed that the position feedback is derived from a measurement of the piston position, x_p. Thus the servovalve command voltage is

$$e = K_x\left(x_{p_c} - x_p\right) - K_p P_F \tag{14}$$

where K_x is the position feedback gain, x_{p_c} is the command signal, and K_p is the pressure feedback gain.

The complete model given by equations (8) to (14) is summarized in equations (15a) to (15g). An auxiliary state variable, x_1, has been introduced to form the high-passed pressure feedback signal to facilitate later analysis.

$$m_p\ddot{x}_p = -\frac{K}{l}\left(\frac{x_p}{l} - \delta\right) - B_V\dot{x}_p - B_c\frac{\dot{x}_p}{|\dot{x}_p|} + AP_L \tag{15a}$$

$$I\ddot{\delta} = -K\left(\delta - \frac{x_p}{l}\right) + K_1\theta - K_2\delta \tag{15b}$$

$$\dot{P}_L = \frac{4\beta_e}{V}\left(-K_cP_L - 12A\dot{x}_p + K_qx_s\right) \tag{15c}$$

$$\dot{x}_s = -\frac{1}{\tau_s}x_s + \frac{K_s}{\tau_s}e \tag{15d}$$

$$\dot{x}_1 = -\frac{1}{\tau_p}x_1 + P_L \tag{15e}$$

$$P_F = P_L - \frac{1}{\tau_p}x_1 \tag{15f}$$

$$e = K_x\left(x_{p_c} - x_p\right) - K_pP_F \tag{15g}$$

DERIVATION OF TRANSFER FUNCTIONS AND APPROXIMATE LITERAL FACTORS

The model equations (eqs. (15a) to (15g)) can be manipulated to form the system open-loop transfer functions. Approximate literal factors of these functions are given in this section. To derive the open-loop transfer functions, linear equations are necessary. The nonlinear terms in the model are the coulomb friction, B_c, and the valve coefficients. Linear approximations for the valve coefficients were given in equations (4a) and (4b) and are assumed in the following analysis. To eliminate B_c it is assumed that a valid model may be retained by setting B_c equal to zero and increasing B_V to provide the required damping at a specific frequency. It is demonstrated later that this is a valid technique.

Equations (15a) to (15d) describe the open-loop system. Incorporating the above assumptions, these equations are Laplace transformed and written in matrix form as

$$\begin{bmatrix} m_ps^2 + B_Vs + \frac{K}{l^2} & -\frac{K}{l} & -A & 0 \\ -\frac{K}{Il} & s^2 + \frac{K + K_2}{I} & 0 & 0 \\ \frac{48\beta_eA}{V}s & 0 & s + \frac{4\beta_eK_c}{V} & -\frac{4\beta_eK_q}{V} \\ 0 & 0 & 0 & \tau_ss+1 \end{bmatrix} \begin{bmatrix} x_p \\ \delta \\ P_L \\ x_s \end{bmatrix} = \begin{bmatrix} 0 & 0 \\ 0 & \frac{K_1}{I} \\ 0 & 0 \\ K_s & 0 \end{bmatrix} \begin{bmatrix} e \\ \theta \end{bmatrix}$$

The determinant of the matrix of coefficients is expanded to give the characteristic equation, and Cramer's rule is used to determine the numerators of the transfer functions. Only transfer functions of response due to command voltage input are given at this time. Open-loop θ transfer functions are of little interest because θ inputs (hinge moments) represent disturbances. Closed-loop transfer functions of response due to θ inputs are considered later.

$$\frac{x_p}{e}(s) = \frac{1}{\Delta(s)} \frac{4\beta_e A K_s K_q}{V} \left(s^2 + \frac{K + K_2}{I} \right) \tag{16}$$

$$\frac{\delta}{e}(s) = \frac{1}{\Delta(s)} \frac{4\beta_e K K_s K_q A}{I l V} \tag{17}$$

$$\frac{P_L}{e}(s) = \frac{1}{\Delta(s)} \frac{4\beta_e K_s K_q}{V} \left\{ m_p s^4 + B_v s^3 + \left[\frac{K}{l^2} + \frac{(K + K_2) m_p}{I} \right] s^2 + \frac{B_v}{I}(K + K_2) s + \frac{K K_2}{I l^2} \right\} \tag{18}$$

where

$$\Delta(s) = (\tau_s s + 1) \left\{ m_p s^5 + \left(\frac{4\beta_e K_c m_p}{V} + B_v \right) s^4 + \left[\frac{(K + K_2) m_p}{I} + \frac{4\beta_e B_v K_c}{V} + \frac{K}{l^2} + \frac{48\beta_e A^2}{V} \right] s^3 + \left[\frac{4\beta_e K_c m_p}{IV}(K + K_2) + \frac{B_v}{I}(K + K_2) + \frac{4\beta_e K K_c}{V l^2} \right] s^2 + \left[\frac{K K_2}{I l^2} + \frac{4\beta_e K_c B_v}{IV}(K + K_2) + \frac{48\beta_e A^2}{IV}(K + K_2) \right] s + \frac{4\beta_e K K_c K_2}{IV l^2} \right\} \tag{19}$$

The above transfer functions are exact for the linear model. Thus, for a specific design, the parameters could be assigned values, and equations (16) to (19) could be used to determine the system response. This could be done easily on a digital computer. However, much insight into the dynamics of the system may be gained if literal expressions for various special cases can be derived. If the resulting literal expressions can be shown to be valid under the assumptions of the derivations, they may be useful in system design and analysis.

For the remainder of this report it is assumed that $m_p << \frac{I}{l^2}$. In the following sections approximate literal transfer functions are derived from equations (16) to (19). The derivations begin with a basic system and become successively more complex. The basic system is obtained by assuming that the piston mass and friction are negligible and that there is no hinge moment. This is the system analyzed in reference 1.

Case I: Basic System

In Case I, the basic system, it is assumed that there is no hinge-moment loading, that the mass of the piston is negligible compared to the load mass, and that friction

forces are negligible. Incorporating these assumptions in equation (19),

$$\Delta(s) = s(\tau_s s + 1)\left[\left(\frac{K}{l^2} + \frac{48\beta_e A^2}{V}\right)s^2 + \frac{4\beta_e K K_c}{Vl^2}s + \frac{48\beta_e A^2 K}{IV}\right]$$

Dividing by the constant term gives

$$\Delta(s) = \frac{48\beta_e A^2 K}{IV}\, s(\tau_s s + 1)\left[\left(\frac{IV}{48\beta_e A^2 l^2} + \frac{I}{K}\right)s^2 + \frac{IK_c}{12A^2 l^2}s + 1\right] \tag{20}$$

Defining

$$\omega_h^2 = \frac{48\beta_e A^2 l^2}{IV} \tag{21}$$

$$\omega_s^2 = \frac{K}{I} \tag{22}$$

$$\frac{1}{\omega_c^2} = \frac{1}{\omega_s^2} + \frac{1}{\omega_h^2} \tag{23}$$

$$\zeta_c = \frac{K_c I}{24A^2 l^2}\,\omega_c \tag{24}$$

gives

$$\Delta(s) = \frac{48\beta_e A^2 K}{IV}\, s(\tau_s s + 1)\left(\frac{s^2}{\omega_c^2} + \frac{2\zeta_c}{\omega_c}s + 1\right)$$

Hence, there is a second-order resonance in the servo response. The factor ω_s may be recognized as the natural frequency of the load coupled with the torque tube spring. The factor ω_h arises because of the compressibility of the hydraulic fluid and is referred to as the hydraulic natural frequency. The two modes couple to give the load resonance, ω_c, and $\omega_c < \omega_s$. The damping of the load resonance, ζ_c, is characteristically small (< 0.1).

The transfer functions (eqs. (16) to (18)) become

$$\frac{x_p}{e}(s) = \frac{1}{\Delta_1(s)}\,\frac{K_s K_q}{12A}\left(\frac{s^2}{\omega_s^2} + 1\right) \tag{25a}$$

$$\frac{\delta}{e}(s) = \frac{1}{\Delta_1(s)} \frac{K_s K_q}{12A\ell} \tag{25b}$$

$$\frac{P_L}{e}(s) = \frac{1}{\Delta_1(s)} \frac{IK_s K_q}{12A^2\ell^2} s^2 \tag{25c}$$

$$\Delta_1(s) = s(\tau_s s + 1)\left(\frac{s^2}{\omega_c^2} + \frac{2\zeta_c}{\omega_c} s + 1\right) \tag{25d}$$

Figure 2 shows this system with the position and pressure feedback loops described by equation (14) incorporated. The $\frac{P_L}{x_p}(s)$ transfer function is the ratio of equation (25c) and equation (25a).

Figure 3 shows the system root locus for the position loop closure and the pressure loop closure. Figure 3(a) shows only the position loop closure. The pole locations, p_1 and p_2, indicate the placement of the closed-loop poles at the desired value of position feedback gain, K_x. If $\omega_c >> p_1$ and $\frac{1}{\tau_s} >> p_1$, the $\frac{x_p}{e}(s)$ transfer function may be approximated by

$$\frac{x_p}{e}(s) = \frac{K_s K_q}{12A} \frac{1}{s}$$

Then the closed-loop $\frac{x_p}{x_{p_c}}(s)$ transfer function becomes

$$\frac{x_p}{x_{p_c}}(s) = \frac{\frac{K_x K_s K_q}{12A}}{s + \frac{K_x K_s K_q}{12A}}$$

and the characteristic first-order hydraulic servo response is obtained with the time constant determined by the position feedback gain, K_x.

If the preceding assumptions are not warranted, the closed-loop pole locations, p_1 and p_2, may be obtained by applying the root-locus-magnitude criterion (ref. 10). If $\omega_c \cong \omega_s$, the quadratics in equation (25a) may be neglected and

$$\frac{x_p}{e}(s) = \frac{K_s K_q}{12As(\tau_s s + 1)}$$

Applying the root-locus-magnitude criterion to determine the pole locations p_1 and p_2 gives

$$\frac{K_x K_s K_q}{12Ap(\tau_s p + 1)} = -1$$

or

$$p^2 + \frac{1}{\tau_s} p + \frac{K_x K_s K_q}{12A\tau_s} = 0$$

and

$$p_{1,2} = -\frac{1}{2\tau_s} \pm \frac{1}{2} \sqrt{\frac{1}{\tau_s^2} - \frac{K_x K_s K_q}{3A\tau_s}}$$

Thus if the quadratic terms may be neglected (i.e., $\omega_c \cong \omega_s$) the closed-loop transfer function following the position loop closure is

$$\frac{x_p}{x_{p_c}}(s) = \frac{K_x K_s K_q}{12A\tau_s (s + p_1)(s + p_2)}$$

If $\omega_c \approx p_1$, figure 3(a) indicates that the position loop closure drives the load resonance mode, ω_c, unstable.

Figure 3(b) indicates the pressure loop closure (following the position loop closure) for two different values of τ_p. The position loop closure has driven the combined resonance unstable and established the location of poles p_1 and p_2. Also, the zeros at ω_s are exactly canceled by poles for the pressure loop closure. The usefulness of DPF in providing damping is largely due to this fact. The smaller value of $\frac{1}{\tau_p}$ gives the best damping performance but is susceptible to static loading errors. In the limit $\frac{1}{\tau_p} = 0$ a simple proportional pressure feedback would result and static load would yield a static position error. As $\frac{1}{\tau_p}$ is increased, however, the efficiency of pressure feedback as a damper decreases. Thus there is an optimum trade-off between the location of the high-pass time constant and the static loading error. Reference 9 recommends placing $\frac{1}{\tau_p}$ at $\frac{1}{3}\omega_c$. Figure 3(b) also shows that as the pressure feedback gain

increases, the pole at $\frac{1}{\tau_p}$ moves toward the origin. This will cause a dipole in the closed-loop $\frac{x_p}{x_{p_c}}(s)$ transfer function at $\frac{1}{\tau_p}$. The residue of this dipole may be large enough to cause a 5° to 10° phase shift in the system frequency response at low frequencies. Such a phase shift is sometimes attributed to unknown nonlinearities when it may be due to the lag-lead characteristic of the dipole. The three zeros at the origin cause two branches of the root locus to approach the origin from the right-half plane at an angle of ±60°. Thus DPF will cause instability of this model at high gains.

Figure 3 also indicates the difficulty of attempting to achieve damping of the load resonance poles with conventional lag-lead compensation. The proximity of the zeros at ω_s to the load resonance poles implies that it would be difficult, if not impossible, to achieve an acceptable design with conventional techniques. By canceling these zeros, DPF eliminates this problem. Also, the cancellation is inherent in DPF, so that exact knowledge of the zero location is not necessary.

Equation (25b) illustrates the necessity of using the piston position as the feedback signal rather than the load position, δ. The presence of the second-order zero in the numerator of $\frac{x_p}{e}(s)$ provides vital phase lead in the region of gain crossover which is not provided by $\frac{\delta}{e}(s)$. This point is illustrated in reference 2.

Case II: Piston Mass and Friction Included

In Case II the restrictions on the piston mass and friction are removed but the load-free case is still considered. These are the conditions which exist during ground testing of an aircraft surface servo. The analysis in the next section, in which hinge-moment loading is included, would apply during actual flight operation.

Rewriting equation (19) with $K_2 = 0$ gives

$$\Delta(s) = s(\tau_s s + 1)\left[m_p s^4 + \left(\frac{4\beta_e K_c m_p}{V} + B_v\right)s^3 + \left(\frac{K m_p}{I} + \frac{4\beta_e B_v K_c}{V} + \frac{K}{l^2} + \frac{48\beta_e A^2}{V}\right)s^2 + \left(\frac{4\beta_e K K_c m_p}{IV} + \frac{K B_v}{I} + \frac{4\beta_e K K_c}{Vl^2}\right)s + \left(\frac{4\beta_e K K_c B_v}{IV} + \frac{48\beta_e A^2 K}{IV}\right)\right] \quad (26)$$

The development of approximate literal factors of the system transfer functions for Cases II and III is given in appendix A. It is shown that if $K_c B_v << 12A^2$, equation (26)

may be factored to give

$$\Delta(s) = s\left(\frac{s^2}{\omega_c^2} + \frac{2\zeta_c}{\omega_c}s + 1\right)\left(\frac{s^2}{\omega_2^2} + \frac{2\zeta_2}{\omega_2}s + 1\right)(\tau_s s + 1) \tag{27}$$

The load resonance, ω_c, is still defined by equation (23), and ω_2 is a high-frequency mode resulting from the inclusion of the piston mass.

The numerators of $\frac{x_p}{e}(s)$ and $\frac{\delta}{e}(s)$ are still given by equations (25a) and (25b). In appendix A the numerator of $\frac{P_L}{e}(s)$ is shown to have the form

$$s(s + z_1)\left(s^2 + 2\zeta_p\omega_p s + \omega_p^2\right)$$

The factors z_1, ω_p, and ζ_p are derived in appendix A on the assumption that $2\zeta_p\omega_p z_1 << \omega_p^2$ and $\frac{K}{l^2 m_p} >> \frac{K}{I}$.

In summary, the open-loop transfer functions are:

$$\frac{x_p}{e}(s) = \frac{1}{\Delta_2(s)}\frac{K_s K_q}{12A}\left(\frac{s^2}{\omega_s^2} + 1\right) \tag{28a}$$

$$\frac{\delta}{e}(s) = \frac{1}{\Delta_2(s)}\frac{K_s K_q}{12A\,l} \tag{28b}$$

$$\frac{P_L}{e}(s) = \frac{1}{\Delta_2(s)}\frac{IK_s K_q}{12A^2 l^2}s(s + z_1)\left(\frac{s^2}{\omega_p^2} + \frac{2\zeta_p}{\omega_p}s + 1\right) \tag{28c}$$

$$\Delta_2(s) = s(\tau_s s + 1)\left(\frac{s^2}{\omega_c^2} + \frac{2\zeta_c}{\omega_c}s + 1\right)\left(\frac{s^2}{\omega_2^2} + \frac{2\zeta_2}{\omega_2}s + 1\right) \tag{28d}$$

$$z_1 = \frac{B_v l^2}{I} \tag{29}$$

$$\omega_p = \frac{K}{l^2 m_p} \tag{30}$$

$$\zeta_p = \frac{B_v}{2m_p}\left(\frac{1}{m_p} - \frac{\ell^2}{I}\right) \tag{31}$$

The inclusion of the piston mass introduces an additional high-frequency mode in the response. This mode is the result of the interaction of the piston and the torque tube spring. The damping of the mode, ζ_2, is proportional to B_v.

The effect of the dynamic pressure feedback will be modified because of the inclusion of friction. The location of the zero at z_1 has a marked effect on the pressure loop closure, as illustrated in figure 4. The position loop has already been closed, and the high-frequency complex poles and zeros at ω_2 and ω_p are neglected. The movement of the poles at ω_2 is negligible for the values of K_x and K_p used to stabilize the load resonance poles. For instance, in the example given later, $\omega_c \approx 50$ rad/sec, $\omega_2 \approx 2000$ rad/sec, and $\omega_p \approx 1500$ rad/sec. Figure 4(a) indicates the closure when $p_1 > z_1$, and figure 4(b) indicates the closure when $p_1 < z_1$. (Both p_1 and z_1 may be near $\frac{1}{\tau_p}$, so this pole location must be considered also.)

Figure 4(a) indicates a damping action similar to that shown in figure 3(b). Figure 4(b), however, shows the load resonance to be much better damped for the same value of K_p, and at larger values of pressure feedback gain, K_p, a low-frequency oscillatory mode emerges. It is suspected that this is the type of response mentioned in reference 8. Furthermore, the high-frequency piston mode, ω_2, is probably the cause of the high-frequency noise also observed in reference 8. There it was stated that the only effective means of eliminating the noise was to introduce friction on the piston. This observation agrees with equation (31), in which the damping of the mode is shown to be proportional to the friction.

Figure 4 indicates that there will again be a dipole in the $\frac{x_p}{x_{p_c}}(s)$ transfer function at $\frac{1}{\tau_p}$, which may cause low-frequency phase lag. Also, the two zeros at the origin cause two branches of the root locus to approach the origin at ±90°. Thus DPF will not cause system instability at high gain as for Case I.

Case III: Hinge Moment Included

Open-loop transfer functions.—In Case III hinge moment is included in the model, resulting in equation (19), the characteristic equation. In appendix A it is shown that if

$$\frac{4\beta_e K_c B_v}{IV}(K + K_2) + \frac{KK_2}{I\ell^2} << \frac{48\beta_e A^2}{IV}(K + K_2)$$

and $p_3 << \omega_c$, equation (19) may be factored to give

$$\Delta(s) = (\tau_s s + 1)(s + p_3)\left(\frac{s^2}{\omega_{ch}^2} + \frac{2\zeta_h}{\omega_{ch}} s + 1\right)\left(\frac{s^2}{\omega_{2h}^2} + \frac{2\zeta_{2h}}{\omega_{2h}} s + 1\right)$$

where the subscript h indicates the effect of hinge moment. It is noted in appendix A that

$$\omega_{ch} = \sqrt{\frac{K + K_2}{K}}\,\omega_c$$

$$\zeta_{ch} = \sqrt{\frac{K + K_2}{K}}\,\zeta_c$$

hence the stability and damping of the load resonance poles of the loaded system will be slightly improved. It is also noted that $\omega_{2h} = \omega_2$ and $\zeta_{2h} = \zeta_2$, indicating the independence of the piston mode from hinge-moment effects.

The numerators of $\frac{x_p}{e}(s)$ and $\frac{\delta}{e}(s)$ remain unchanged, but $\frac{P_L}{e}(s)$ must be reconsidered. Appendix A indicates that the numerator of $\frac{P_L}{e}(s)$ may be approximated by

$$\left(s^2 + 2\zeta_{ph}\omega_{ph} s + 1\right)\left(s^2 + 2\zeta_t\omega_t s + \omega_t^2\right)$$

if $\frac{K + K_2}{I} << \frac{K}{l^2 m_p}$ and $\omega_t << \omega_{ph}$.

In the preceding expression

$$\omega_{ph} \cong \omega_p$$

$$\zeta_{ph} \cong \zeta_p$$

$$\omega_t = \sqrt{\frac{K_2}{I}}$$

$$\zeta_t = \frac{1}{2}\,\frac{l^2 B_v}{I}\sqrt{\frac{I}{K_2}}$$

The factored transfer functions for Case III are given in table 1. The simplified models of Cases I and II (eqs. (25a) to (25d) and (28a) to (28d)) may be obtained by setting m_p, B_v, or K_2 equal to zero. The subscript h has been eliminated from the parameters in table 1.

Figure 5 shows the pressure loop closure (following the position loop closure) for Case III. The load resonance poles at ω_c will close on the zeros at ω_t. Thus the location of these zeros is critical to the stability of the system. If they lie in the region of ω_c, DPF will be ineffective as a damper. Table 1 shows that ω_t is proportional to the square root of the hinge moment, K_2, and that ζ_t is proportional to B_v. Thus some amount of friction on the piston is desirable, because it causes the zeros at ω_t to move toward a region of higher damping. Of course, piston friction is also needed to supply damping for the high-frequency mode at ω_2. Also, the low-frequency oscillatory mode which occurs at high DPF gains and low values of position loop gains (fig. 4(b)) does not occur with hinge-moment loading.

Hinge-moment loading errors.—Only open-loop transfer functions of system response due to a command voltage input have been considered. These transfer functions and their approximate literal factors, which have been developed, should make it possible to design a system with a suitable closed-loop response. Once this has been accomplished, the sensitivity of the closed-loop system to hinge-moment loading is of interest. To study this effect, the $\frac{\delta}{\theta}(s)$ transfer function of the closed-loop system will be determined. Thus the open-loop matrix used to derive the open-loop transfer functions must be augmented by the control law (eqs. (15e) to (15g)). The voltage signal is now

$$e = K_x(x_{p_c} - x_p) - K_p P_F$$

$$= K_x(x_{p_c} - x_p) - K_p P_L + \frac{1}{\tau_p} K_p x_1$$

and the $\dot{x}_s$ equation becomes

$$\tau_s \dot{x}_s = - x_s + K_s\left(K_x x_{p_c} - K_x x_p - K_p P_L + \frac{1}{\tau_p} K_p x_1\right)$$

where

$$\dot{x}_1 = - \frac{1}{\tau_p} x_1 + P_L$$

Using the last two equations, the closed-loop system matrix is

$$\begin{bmatrix} m_p s^2 + B_v s + \frac{K}{l^2} & -\frac{K}{l} & -A & 0 & 0 \\ -\frac{K}{lI} & s^2 + \frac{K + K_2}{I} & 0 & 0 & 0 \\ \frac{48\beta_e A}{V} s & 0 & s + \frac{4\beta_e K_c}{V} & -\frac{4\beta_e K_q}{V} & 0 \\ K_s K_x & 0 & K_s K_p & \tau_s s + 1 & -K_s K_p \frac{1}{\tau_p} \\ 0 & 0 & -1 & 0 & s + \frac{1}{\tau_p} \end{bmatrix} \begin{bmatrix} x_p \\ \delta \\ P_L \\ x_s \\ x_1 \end{bmatrix} = \begin{bmatrix} 0 & 0 \\ 0 & \frac{K_1}{I} \\ 0 & 0 \\ K_s K_x & 0 \\ 0 & 0 \end{bmatrix} \begin{bmatrix} x_{p_c} \\ \theta \end{bmatrix} \quad (32)$$

The numerator of the $\frac{\delta}{\theta}(s)$ transfer function is

$$\frac{K_1}{I}\left\{\left(m_p s^2 + B_v s + \frac{K}{l^2}\right)\left[\left(s + \frac{4\beta_e K_c}{V}\right)(\tau_s s + 1)\left(s + \frac{1}{\tau_p}\right) + \frac{4\beta_e K_q K_s K_p}{V} s\right]\right. \quad (33)$$
$$\left. + A\left(s + \frac{1}{\tau_p}\right)\left[\frac{48\beta_e A}{V} s\left(\tau_s s + 1\right) + \frac{4\beta_e K_q K_s K_x}{V}\right]\right\}$$

Unfortunately, there are no simple literal factors of equation (33). It is a complex function of the feedback quantities K_x, K_p, and τ_p. It is possible to calculate the static closed-loop load position, δ, due to hinge-moment loading by computing only the constant term of the $\frac{\delta}{\theta}(s)$ transfer function. Equation (33) provides the numerator constant, and the system matrix furnishes the denominator constant:

$$\left[\frac{\delta}{\theta}(s)\right]_{ss} = \frac{KK_1K_c + l^2K_1K_qK_sK_xA}{KK_2K_c + l^2(K + K_2)K_qK_sK_xA}$$

This expression gives the exact steady-state hinge-moment loading error. If the terms involving K_c are neglected,

$$\left[\frac{\delta}{\theta}(s)\right]_{ss} \approx \frac{K_1}{K + K_2}$$

This result could have been anticipated, because the high-pass filter in the pressure feedback loop isolates the load from closed-loop dynamics in the steady state. For a

specific problem, the system constants may be inserted into equation (33), and the resulting polynomial may be factored to give the frequency dependence of the hinge-moment loading error.

COMPARISON OF GPAS RUDDER AND MODEL RESPONSE

GPAS Rudder Electrohydraulic Servo

The GPAS is a variable-stability JetStar airplane operated by the NASA Flight Research Center. The basic control surfaces were disconnected from the left-hand pilot's controllers, and irreversible electrohydraulic servos were installed. Thus the control-surface positions may be electrically controlled for airborne simulation purposes. Details of the GPAS system are given in reference 11. The GPAS rudder is used in the following discussions to illustrate the analysis presented in the previous sections. Thus the surface deflection, δ, of the previous sections becomes the rudder deflection, δ_r, and the angle θ is interpreted as the aircraft sideslip angle, β.

Figure 6 shows the location of the rudder hydraulic actuator and its relationship to the rudder surface. The electrohydraulic system consists of a servovalve, which controls fluid flow to the double-ended hydraulic actuator. The system operating pressure is 3000 psi. The rudder surface is mass-balanced. The constants required in equations (15a) to (15g) for the rudder model are given in table 2. Appendix B discusses the problems encountered in determining these constants. In order to install the servo, the rudder torque tube had to be cut and the moment arm linkage had to be inserted. In the basic JetStar there was no power boost to the rudder, and in the GPAS modification the rudder is permanently connected by cables to the right-hand pilot's rudder pedals. It was not necessary to include these rudder pedals (an extra mass-spring system) in the analysis.

An electrical pressure transducer is used to provide the pressure feedback signal. Figure 6 shows that several feet of hydraulic tubing are required to connect the servo valve, the pressure transducer, and the actuator. In recent years it has become common to use an integral servo valve/actuator system with built-in mechanical position and pressure feedbacks. Such units are useful for large installations and for specific applications, because major mechanical modifications are necessary to alter the system characteristics. For small installations, the versatility of electrical feedback signals may be important. Either method will provide the same system characteristics. The rudder position transducer is a rotary potentiometer located beneath the actuator and strapped around the torque tube (fig. 7).

Early testing of the rudder servo revealed a stair-stepping response to a step input command. It was recognized that the response was caused by the static friction on the piston. The problem was solved by superimposing a constant-amplitude, 60-hertz dither signal on the command signal. The amplitude of the dither signal was adjusted to effectively "break" the static friction while leaving the overall response unchanged. Hence, only coulomb friction, B_c, is included in this analysis.

Rudder and Model Response

To compare the rudder response with the model response, the model equations of motion (eqs. (15a) to (15g)) with the constants given in table 2 were mechanized on an analog computer, and step and frequency responses were obtained. Two nonlinearities were programed: the valve flow-pressure coefficient, K_c, and the coulomb friction, B_c. Equations (4a) and (4b) or (5a) and (5b) were used for the valve coefficients, K_c and K_q. Thus a function switch selected either equation (4b) or equation (5b) as the term included in the pressure equation. The coulomb friction, B_c, could be eliminated by setting a potentiometer to zero. As indicated in the section on DERIVATION OF TRANSFER FUNCTIONS AND APPROXIMATE LITERAL FACTORS, the viscous friction coefficient, B_v, may then be increased to yield the desired damping at a prescribed frequency. For the linear model, B_v was increased from 500 lb/ft-sec^{-1} to 2000 lb/ft-sec^{-1}. A linear model is desirable because root loci and frequency response analysis techniques may then be used. Thus it is important to verify the suitability of the linear model. A digital program, CONTROL, which is described in appendix C, was used to calculate the root loci and frequency responses of the linear model.

The step and frequency responses of the rudder and the nonlinear model are given in figures 8 to 10. The rudder tests were made on the ground, so there was no hinge-moment loading. The test input was always a 1° command. All responses were obtained with K_x = 1090 V/ft. The pressure feedback gain, K_p, and the time constant of the high-pass circuit, τ_p, were varied. Figure 8 shows the step response of the rudder and the model for $\frac{1}{\tau_p}$ = 8.3, 16.6, and 33.2 rad/sec. Values of K_p range from 0.0048 V/psi to 0.0131 V/psi. At values of K_p less than approximately 0.004 V/psi the response becomes unstable. The 60-hertz oscillation in the rudder response in figure 8(a) may be caused by the dither signal. The agreement between the rudder and nonlinear model step responses shown in figures 8(a) to 8(c) is considered good.

Frequency responses of the rudder, the nonlinear model, and the linear model for two different values of K_p and τ_p are shown in figures 9 and 10. In figures 9(a) and 9(b) the load resonance at approximately 7.5 hertz is evident. Note also the characteristic first-order lag low-frequency attenuation, and the notch characteristic at $f \approx 12$ hertz. The first-order lag characteristic can be explained as follows: The peak at 7.5 hertz and the notch characteristic at 12 hertz are caused by a pair of complex poles and zeros with very low damping ratios. These poles and zeros cannot yield the lower frequency phase attenuation shown in the figures. This phase shift is caused by the real pole, p_1 (fig. 3(a)).

In figures 10(a) and 10(b) the load resonance was damped by the larger pressure feedback, K_p. The agreement between the rudder and model frequency responses in figures 9 and 10 reflects the agreement in the step responses.

Figures 9 and 10 also indicate that only slight differences exist between the linear and nonlinear models. The main difference is in the low-frequency phase shift, where the nonlinear model has more phase shift than the linear model. The rudder phase shift curve is considerably below those of both models at low frequencies. This is especially true with the high damping shown in figures 10(a) and 10(b). This may be caused by nonlinear effects not included in the model. Possible sources of the phase shift are torque motor hysteresis, first-stage servovalve backlash, or actuator static coulomb friction.

Figures 8 to 10 indicate that the rudder servosystem is approximated well by the nonlinear model and that the linear model is a valid approximation of the nonlinear model. Thus a study of the utility of DPF with the linear model would allow more general conclusions to be drawn with regard to the damping action of DPF.

The effect of hinge-moment loading of the rudder surface is shown as a final check of the model in figure 11. Figure 11(a) shows the rudder ground test step response, and figure 11(b) shows a step response recorded during flight. The loading causes the servo to be better damped, and the resonant frequency (in the step response) increases. Figures 12(a) and 12(b) show the step response of the nonlinear model with and without hinge-moment loading. Inspection of these responses leads to the same conclusions as were drawn from figure 11.

Table 3 compares the approximate literal factors developed in the analysis section for Cases I, II, and III to the exact values obtained with the CONTROL program. In Case I the literal factors are exact. In Cases II and III the approximate factors are close enough to the exact values to make a first analysis possible. For the rudder model $\frac{I}{l^2} = 72$ slugs and $m_p = 0.166$ slug. Thus the condition $m_p << \frac{I}{l^2}$ is satisfied.

Table 3 also shows that the high-frequency poles at ω_2 are overdamped. Thus there should be no high-frequency control-valve-generated noise ("honk") in the system. The damping is attributed to the large value of B_V. Of course, B_V was adjusted to match the system's response at the load resonance frequency (approximately 50 rad/sec). Thus a separate calculation with a lower value of B_V (corresponding to the higher frequency ω_2) may be in order to estimate the damping of this high-frequency mode more accurately.

ANALYSIS OF DYNAMIC PRESSURE FEEDBACK

The effect of dynamic pressure feedback on system stability was analyzed, using the GPAS rudder servo for illustration. In addition, the effects of K_X, K_p, and $\frac{1}{\tau_p}$ on cases I, II, and III were studied.

The CONTROL program was used to obtain the root loci of the linear rudder model

for the three cases with K_x, K_p, and $\frac{1}{\tau_p}$ as parameters. The loci are plotted in figure 13. Loci of the load resonance poles are plotted for three values of $\frac{1}{\tau_p}$ and four values of K_x. Only the third quadrant of the s plane is shown. Dots along the loci indicate gain increments of $\Delta K_p = 0.00348$ V/psi.

Figure 13(a) gives the loci for Case I. The GPAS system design called for a closed-loop rudder servo bandwidth of 50 rad/sec. This goal is most closely achieved by the position feedback gain, K_x, of 1090 V/ft and is the value used in the system. This value of K_x places p_1 at 42 rad/sec; however, this system would be objectionable because of the limited damping action of the DPF gain, K_p. Figure 13(a) also illustrates a point made in connection with figure 3(b)--that high K_p gains may drive the system unstable. Figure 13(a) shows that better damping performance can be achieved by reducing the position feedback gain, K_x, with the attendant loss in system bandwidth. This model of the system (Case I) is unrealistic because friction on the piston was neglected.

Figure 13(b) gives the loci for Case II. The damping for $K_x = 1090$ V/ft is reasonable, and, again, as K_x decreases, the damping performance of the DPF improves. When $K_x = 436$ V/ft and 654 V/ft, the effect is the same as that noted in figure 4(b), where $p_1 < z_1$ and a low-frequency oscillatory mode emerges at low values of $\frac{1}{\tau_p}$ as K_p increases. If K_p were increased from zero, the load resonance oscillations would become well damped (they would, in fact, disappear), leaving a desirable step response. If K_p were increased still further, the low-frequency mode would appear in the response.

Figures 13(a) and 13(b) indicate that for many designs there will be a value of K_p beyond which DPF does not increase damping; in fact, damping may decrease. More importantly, DPF will then also reduce the system bandwidth (through the frequency of the load resonance poles).

Figure 13(c) gives the loci for Case III. The load resonance poles at ω_c close on the zeros at ω_t. Differences between figures 13(b) and 13(c) illustrate the difference that may be expected between ground tests and flight operation of aircraft hydraulic servos. The frequency of the load resonance poles is lower in figure 13(b) (56 rad/sec to 58 rad/sec) than in figure 13(c) (62 rad/sec to 64 rad/sec). This could have been anticipated by noting from table 1 that ω_c increases as K_2 increases. In figure 13(c) there is a maximum damping that is practical. The loci for the different values of K_x are similar, and all yield acceptable damping. In addition, the change in the loci of figure 13(c) for changes in τ_p is small relative to the larger changes of figure 13(b).

Also, increments of K_p in figure 13(c) cause smaller load resonance pole motion than in figure 13(b).

The root loci of figures 13(a) to 13(c) give insight into the behavior of the load resonance poles. To augment this information, the closed-loop frequency response of the system indicates the system bandwidth, phase margin, and low-frequency phase shifts. Figures 14 and 15 give the frequency response of the linear rudder model for variations in K_x and K_p with τ_p held constant at $\frac{1}{\tau_p} = 16.6$ rad/sec. The hinge-moment coefficient, K_2, was set at zero, which corresponds to the ground test value. In figures 14(a) and 14(b), in which $K_p = 0.00348$ V/psi, K_x has strong control over the resonant peak at 7 hertz to 8 hertz. However, lowering K_x also lowers the bandwidth (fig. 14(b)). In figures 15(a) and 15(b), in which $K_x = 1090$ V/ft and K_p is varied, K_p does not exercise strong control over the magnitude of the resonance, but it does draw the resonance to lower frequencies (fig. 13(b)).

Figures 16(a) and 16(b) illustrate the change in closed-loop response when hinge-moment loading is included. When hinge moment is included, the frequency of the resonance peak increases, its magnitude decreases, and the phase margin increases. These effects bear out the comments made in connection with figures 11 and 12.

The following conclusions about the damping action of DPF may be drawn from figures 13 to 16. If ω_c is in the frequency region of the desired closed-loop bandwidth, the position loop closure will drive the load resonance poles toward the unstable region. With $\frac{1}{\tau_p}$ set at approximately $\frac{1}{3}\omega_c$, DPF will always have some damping effect and will usually be quite effective. However, if K_x is large, the resulting DPF damping action may not be satisfactory. Decreasing K_x always allows better damping action by DPF, but this causes a loss of bandwidth. There will usually be a value of K_p beyond which DPF does not increase damping (it may, in fact, decrease damping) and directly lowers the closed-loop bandwidth. Inclusion of hinge-moment loading decreases the sensitivity of the load resonance poles to variations in K_x, K_p, and τ_p. In addition, it raises the frequency of the load resonance, lowers the magnitude of the resonance peak, and increases the phase margin. Thus, the operation of the system will be more stable during flight than during ground operation.

The use of DPF in an aircraft control-surface servosystem makes the system sensitive to variations in hinge-moment loading. Hinge-moment loads arise out of the variations in the angle of incidence at the surface caused by aircraft maneuvers, control-surface deflection, or atmospheric turbulence. Whether any of these effects unduly compromise the servo response is considered in the following discussion.

For the aircraft rudder servo being analyzed, load variations are attributed to

changes in sideslip angle, β, rudder deflection, δ_r, and turbulence, β_g. The response of an aircraft to a rudder step is caused primarily by the excitation of the Dutch roll mode. Ignoring the effect of the roll and spiral modes, the response of the GPAS to a rudder step for a selected flight condition can be expressed as

$$\frac{\beta}{\delta_r}(s) = \frac{1.76}{s^2 + 0.265s + 2.4}$$

This function was mechanized in the analog simulation, and the nonlinear rudder model was used to obtain the time history shown in figure 17. The frequency of the load variation was small enough so that the rudder servo was able to maintain constant commanded x_p following the initial transient; however, the rudder surface position, δ_r, varied as it was forced by β. Because the frequency of the Dutch roll oscillation was much less than the bandwidth of the servo, the variation in δ_r may be approximated by

$$\Delta\delta_r \approx \left(\frac{\delta}{\theta}\right)_{ss} \Delta\beta$$

Load variations will also be caused by atmospheric turbulence. Lateral gust velocity, v_g, induces an effective incremental sideslip of $\beta_g = \frac{v_g}{V_a}$ and will be sensed by the servosystem as a changing hinge moment. The response of the rudder to turbulence was simulated using the gust power spectra:

$$\Phi_{v_g}(\omega) = \frac{\sigma_g^2 L_g}{\pi V_a} \frac{\left[1 + 3\left(\frac{L_g}{V_a}\right)^2 \omega^2\right]}{\left[1 + \left(\frac{L_g}{V_a}\right)^2 \omega^2\right]^2}$$

where V_a is the aircraft velocity, L_g is the turbulence scale factor, and σ_g is the root-mean-square gust velocity. This power spectrum may be realized by passing white noise through an appropriate shaping filter.

Figure 18 shows the GPAS rudder servo response to turbulence at a cruise flight condition. A moderate turbulence level of $\sigma_g = 5$ ft/sec was used. The ratio $\frac{L_g}{V_a}$ was set at 10 seconds. The response of δ_r indicates that the response of the servo to load variations caused by atmospheric turbulence is acceptable.

CONCLUSIONS

A lumped parameter, two-mass system driven by an electrohydraulic servo valve was analyzed. The results of the analysis of a model of the system were compared with test results from a highly resonant rudder electrohydraulic control system. The comparison led to the following conclusions:

1. The model equations of motion accurately represented the test system. The calculated model root loci, frequency responses, and step responses agreed well with test results. A linear model agreed well with a nonlinear model that included the nonlinear flow equation of the servo valve and coulomb friction on the actuator.

2. Approximate literal transfer functions yielded accuracy acceptable for initial analysis if the piston mass was much less than the effective load mass.

3. The system response was characterized by a load resonance and a piston-hydraulic mode. If there was insufficient friction on the piston, the high-frequency piston-hydraulic mode may have been underdamped and could have caused high-frequency control-valve-generated noise referred to as "honk."

4. When the position loop was closed, the load resonance poles were driven toward the unstable region. By locating the high-pass time constant of the pressure feedback at approximately one-third of the load resonance frequency, dynamic pressure feedback (DPF) always provided damping for the load resonance pole. However, if the position feedback gain were too high, damping provided by DPF may have been insufficient.

5. A maximum practical DPF gain usually existed. Increasing the DPF gain beyond this point directly lowered the system bandwidth and possibly decreased the damping.

6. Operation with hinge-moment loads (corresponding to flight operations) resulted in a higher load resonance frequency, smaller frequency response peaking, and increased phase margin than when hinge-moment loading was not included.

7. Hinge-moment loading reduced the sensitivity of the load resonance poles to variations in position and pressure feedback gains and in the high-pass time constant.

8. The response of the rudder servo to load variations caused by atmospheric turbulence was acceptable.

Flight Research Center,

National Aeronautics and Space Administration,

Edwards, Calif., March 3, 1972.

APPENDIX A

DETERMINATION OF MODEL CONSTANTS

In the determination of the constants in table 2 some difficulties were encountered. Although the load moment of inertia, I, and the piston mass, m_p, should be relatively accurately determined quantities, a problem may arise in deciding the location of the spring, K. This location will obviously affect m_p and I. If a distributed spring is encountered, the lumped-parameter model of this report may be completely inappropriate.

The spring constant, K, should be accurately determined, because it is directly related to ω_s, the load resonance frequency. Equation (25a) indicates that $\frac{x_p}{e}(s)$ has a notch characteristic at ω_s. Thus K may be determined by calculation, measurement, or (knowing I) determination of ω_s.

The friction, B_v and B_c, may be experimentally determined with low-frequency triangular wave inputs to the closed-loop system.

It was not necessary to include the rate limit in the servo analysis. Electronic safety trip circuits cut off the GPAS hydraulic system before this rate limit is encountered, and rate limiting is rarely encountered in the operation of the system. This reflects the fact that $P_L << P_s$.

The valve quantities K_s, K_q, K_c, and τ_s can be obtained from manufacturer's data. The first-stage servo valve gain, K_s, is a temperature-dependent quantity because of its dependence on the coil resistance, R. The resistance of copper wire increases by 22 percent in rising from 68° F to 167° F. Thus, the valve gain, K_s, which is inversely proportional to R, will decrease by 18 percent during this temperature rise. Because K_s is a factor in the position loop gain, the servo response will also deteriorate. This problem may be sidestepped by using current to drive the servovalve.

The bulk modulus of elasticity of the hydraulic fluid is difficult to estimate. Handbook values of $\beta_e \cong 250{,}000$ psi for typical petroleum-based fluids are usually too high. In reference 6 the strong dependence of β_e on entrapped air and container compliance is illustrated. At the high pressures used in aircraft hydraulic systems, entrapped air will be dissolved soon after the system begins to operate. However, reference 7 indicates that entrapped air may still cause problems: Dissolved air may come out of solution when the fluid passes through a valve orifice due to the pressure drop. Reference 6 states that a β_e of 100,000 psi yielded good results for many studies. The value used in this report, $\beta_e = 50{,}000$ psi, was determined by attempting

to match the analog simulation response to the measured response. It is believed that values of β_e between these two values will give good results in analyses of hydraulic systems. The value used in an analysis may be chosen according to the relative amount of hydraulic tubing and connections contained in the system. The rudder control system analyzed in this report contained a relatively large amount of tubing and connections, and the smaller value of β_e produced good results. On a close-coupled installation (for instance, with the servovalve mounted on the actuator) the larger value recommended in reference 6 would be appropriate.

APPENDIX B

DEVELOPMENT OF APPROXIMATE LITERAL TRANSFER FUNCTIONS

The approximate literal transfer functions for Cases II and III are developed in this appendix.

CASE II: PISTON MASS AND FRICTION INCLUDED

In Case II the restrictions on the piston mass and friction are removed, and the hinge-moment loading is neglected.

Rewriting equation (19) with K_2 equal to zero gives

$$\Delta(s) = s(\tau_s s + 1)\left[m_p s^4 + \left(\frac{4\beta_e K_c m_p}{V} + B_v\right)s^3 + \left(\frac{K m_p}{I} + \frac{4\beta_e B_v K_c}{V} + \frac{K}{l^2} + \frac{48\beta_e A^2}{V}\right)s^2\right.$$

$$\left. + \left(\frac{4\beta_e K K_c m_p}{IV} + \frac{K B_v}{I} + \frac{4\beta_e K K_c}{V l^2}\right)s + \left(\frac{4\beta_e K K_c B_v}{IV} + \frac{48\beta_e A^2 K}{IV}\right)\right] \qquad (36)$$

In the constant term

$$\frac{4\beta_e K K_c B_v}{IV} << \frac{48\beta_e A^2 K}{IV}$$

or

$$K_c B_v << 12A^2$$

will usually prevail. Hence, dropping the first term of the constant and dividing through by the remaining term,

$$\Delta(s) = \frac{48\beta_e A^2 K}{IV} s(\tau_s s + 1)\left[\frac{IV m_p}{48\beta_e A^2 K} s^4 + \left(\frac{I m_p K_c}{12A^2 K} + \frac{IV B_v}{48\beta_e A^2 K}\right)s^3\right.$$

$$\left. + \left(\frac{V m_p}{48\beta_e A^2} + \frac{I B_v K_c}{12A^2 K} + \frac{IV}{48\beta_e A^2 l^2} + \frac{I}{K}\right)s^2 + \left(\frac{m_p K_c}{12A^2} + \frac{B_v V}{48\beta_e A^2} + \frac{I K_c}{12A^2 l^2}\right)s + 1\right] \qquad (37)$$

This expression has the form

$$\left(\frac{s^2}{\omega_c^2} + \frac{2\zeta_c}{\omega_c}s + 1\right)\left(\frac{s^2}{\omega_2^2} + \frac{2\zeta_2}{\omega_2}s + 1\right) = \frac{s^4}{\omega_c^2\omega_2^2} + \left(\frac{2\zeta_2}{\omega_c^2\omega_2} + \frac{2\zeta_c}{\omega_c\omega_2^2}\right)s^3$$

$$+ \left(\frac{1}{\omega_c^2} + \frac{1}{\omega_2^2} + \frac{4\zeta_2\zeta_c}{\omega_c\omega_2}\right)s^2 + \left(\frac{2\zeta_c}{\omega_c} + \frac{2\zeta_2}{\omega_2}\right)s + 1 \tag{38}$$

The last two terms of the coefficient of s^2 in equation (37) may be recognized as the quantity already defined as $\frac{1}{\omega_c^2}$ in equation (23). Then the coefficient of s^4 in equation (37) is

$$\omega_c^2\omega_2^2 = \frac{48\beta_e A^2 K}{IVm_p}$$

which may be solved for ω_2^2 (using equation (23) for ω_c) as

$$\omega_2^2 = \frac{VK + 48\beta_e A^2 l^2}{Vl^2 m_p}$$

To determine ζ_2, $K_c << 1$. (See table 2.) Hence, setting K_c equal to zero in equation (37) and observing the coefficients of s^3 and s (where ζ_2 occurs) results in the expressions

$$\frac{2\zeta_c}{\omega_c\omega_2^2} + \frac{2\zeta_2}{\omega_2\omega_c^2} = \frac{IVB_v}{48\beta_e A^2 K} \tag{39}$$

and

$$\frac{2\zeta_c}{\omega_c} + \frac{2\zeta_2}{\omega_2} = \frac{B_v V}{48\beta_e A^2} \tag{40}$$

(Although ζ_2 also occurs in the coefficient of s^2 in equation (38), that coefficient is dominated by the other terms in the coefficient.)

The load resonance, ω_c, remains in the vicinity of the $j\omega$ axis near the zero at ω_s as shown in figure 3(a). Thus $\zeta_c \ll 1$, whereas $\zeta_2 \approx 1$. Setting ζ_c equal to zero and solving equations (39) and (40) gives

$$\zeta_2 = \frac{VB_v}{96\beta_e A^2}\left(\frac{I}{K}\right)\omega_c^2\omega_2 \tag{41}$$

$$\zeta_2 = \frac{VB_v}{96\beta_e A^2}\omega_2$$

Because $\omega_c^2 \approx \frac{K}{I}$ these expressions are nearly equivalent and equation (41) will be used to compute ζ_2.

The numerators of $\frac{x_p}{e}(s)$ and $\frac{\delta}{e}(s)$ are still given by equations (25a) and (25b) and do not require further analysis. The numerator of $\frac{P_L}{e}(s)$ does require further analysis. Setting K_2 equal to zero in equation (18), the numerator of $\frac{P_L}{e}(s)$ contains the expression

$$s\left[s^3 + \frac{B_v}{m_p}s^2 + \left(\frac{K}{l^2 m_p} + \frac{K}{I}\right)s + \frac{B_v K}{I m_p}\right] \tag{42}$$

This expression has the form

$$s(s + z_1)\left(s^2 + 2\zeta_p\omega_p s + \omega_p^2\right) = s\left[s^3 + (z_1 + 2\zeta_p\omega_p)s^2\right.$$

$$\left. + \left(2\zeta_p\omega_p z_1 + \omega_p^2\right)s + z_1\omega_p^2\right] \tag{43}$$

In Case I the $\frac{P_L}{e}(s)$ numerator contained s^2. Assuming that the low-frequency response will not be grossly affected by setting $m_p \neq 0$ and $B_v \neq 0$, it is anticipated that z_1 will be small and ω_p will be large. Therefore,

$$2\zeta_p\omega_p z_1 \ll \omega_p^2$$

Comparing the coefficients of the first power of s in equations (42) and (43) results in the expression

$$\omega_p^2 = \frac{K}{\ell^2 m_p} + \frac{K}{I} \cong \frac{K}{\ell^2 m_p} \tag{44}$$

since $\frac{K}{\ell^2 m_p} >> \frac{K}{I}$.

Then the constant terms of equations (42) and (43) give

$$\omega_p^2 z_1 = \frac{B_v K}{I m_p}$$

or

$$z_1 = \frac{B_v \ell^2}{I} \tag{45}$$

To find ζ_p the coefficients of s^2 are equated:

$$z_1 + 2\zeta_p \omega_p = \frac{B_v}{m_p}$$

$$\zeta_p = \frac{1}{2\omega_p}\left(\frac{B_v}{m_p} - z_1\right) = \frac{B_v}{2\omega_p}\left(\frac{1}{m_p} - \frac{\ell^2}{I}\right) \tag{46}$$

In summary, the open-loop transfer functions are:

$$\frac{x_p}{e}(s) = \frac{1}{\Delta_2(s)} \frac{K_s K_q}{12A}\left(\frac{s^2}{\omega_s^2} + 1\right) \tag{47a}$$

$$\frac{\delta}{e}(s) = \frac{1}{\Delta_2(s)} \frac{K_s K_q}{12A\ell} \tag{47b}$$

$$\frac{P_L}{e}(s) = \frac{1}{\Delta_2(s)} \frac{IK_s K_q}{12A^2\ell^2} s(s + z_1)\left(\frac{s^2}{\omega_p^2} + \frac{2\zeta_p}{\omega_p} s + 1\right) \tag{47c}$$

$$\Delta_2(s) = s(\tau_s s + 1)\left(\frac{s^2}{\omega_c^2} + \frac{2\zeta_c}{\omega_c} s + 1\right)\left(\frac{s^2}{\omega_2^2} + \frac{2\zeta_2}{\omega_2} s + 1\right) \tag{47d}$$

where

$$z_1 = \frac{B_v l^2}{I} \qquad \omega_2^2 = \frac{VK + 48\beta_e A^2 l^2}{V l^2 m_p}$$

$$\omega_p^2 = \frac{K}{l^2 m_p} \qquad \omega_s^2 = \frac{K}{I}$$

$$\zeta_p = \frac{B_v}{2\omega_p}\left(\frac{1}{m_p} - \frac{l^2}{I}\right) \qquad \omega_h^2 = \frac{48\beta_e A^2 l^2}{IV}$$

$$\zeta_2 = \frac{VB_v}{48\beta_e A^2 K}\left(\frac{I}{K}\right)\omega_c^2\omega_2 \qquad \frac{1}{\omega_c^2} = \frac{1}{\omega_s^2} + \frac{1}{\omega_h^2}$$

CASE III: HINGE MOMENT INCLUDED

In Case III the restriction on the hinge moment is removed, giving equation (19), a characteristic equation. In the coefficient of s it is noted that usually

$$\frac{4\beta_e K_c B_v}{IV}(K + K_2) + \frac{KK_2}{Il^2} << \frac{48\beta_e A^2}{IV}(K + K_2)$$

Thus, neglecting the first two terms of the coefficient of s in equation (19) and dividing through by the remaining term gives

$$\frac{48\beta_e A^2(K + K_2)}{IV}(\tau_s s + 1)\left\{\frac{IVm_p}{48\beta_e A^2(K + K_2)}s^5 + \left[\frac{IK_c m_p}{12A^2(K + K_2)} + \frac{IVB_v}{48\beta_e A^2(K + K_2)}\right]s^4\right.$$

$$+ \left[\frac{Vm_p}{48\beta_e A^2} + \frac{IB_v K_c}{12A^2(K + K_2)} + \frac{IVK}{48\beta_e A^2 l^2(K + K_2)} + \frac{I}{K + K_2}\right]s^3$$

$$\left. + \left[\frac{K_c m_p}{12A^2} + \frac{VB_v}{48\beta_e A^2} + \frac{IKK_c}{12A^2 l^2(K + K_2)}\right]s^2 + s + \frac{KK_2K_c}{12A^2 l^2(K + K_2)}\right\} \qquad (48)$$

This expression has the form

$$\left(\frac{s^2}{\omega_{ch}^2} + \frac{2\zeta_{ch}}{\omega_{ch}}s + 1\right)\left(\frac{s^2}{\omega_{2h}^2} + \frac{2\zeta_{2h}}{\omega_{2h}}s + 1\right)(s + p_3)$$

where the subscript h indicates the effect of hinge moment.

It is obvious that

$$p_3 = \frac{KK_2K_c}{12A^2l^2(K + K_2)} \tag{49}$$

The factor p_3 is small compared to the other factors in the expression. Thus factoring the root $(s + p_3)$ from equation (48) leaves an expression very similar to equation (37):

$$\frac{48\beta_eA^2(K + K_2)}{IV}(\tau_s s + 1)(s + p_3)\left\{\frac{IVm_p}{48\beta_eA^2(K + K_2)}s^4 + \left[\frac{IK_cm_p}{12A^2(K + K_2)} + \frac{IVB_v}{48\beta_eA^2(K + K_2)}\right]s^3\right.$$
$$+ \left[\frac{Vm_p}{48\beta_eA^2} + \frac{IB_vK_c}{12A^2(K + K_2)} + \frac{IVK}{48\beta_eA^2l^2(K + K_2)} + \frac{I}{K + K_2}\right]s^2$$
$$\left. + \left[\frac{K_cm_p}{12A^2} + \frac{VB_v}{48\beta_eA^2} + \frac{IKK_c}{12A^2l^2(K + K_2)}\right]s + 1\right\}$$

Because of the similarity between this expression and the expression in equation (37), the procedure is exactly the same as that in Case II, that is, identify

$$\omega_{sh}^2 = \frac{K + K_2}{I}$$

$$\omega_{hh}^2 = \frac{48\beta_eA^2l^2(K + K_2)}{IVK}$$

$$\frac{1}{\omega_{ch}^2} = \frac{1}{\omega_{sh}^2} + \frac{1}{\omega_{hh}^2}$$

$$\zeta_{ch} = \frac{IK_cK}{24A^2l^2(K + K_2)}\omega_{ch}$$

$$\omega_{2h}^2 = \frac{VK + 48\beta_eA^2l^2}{IVl^2m_p}$$

$$\zeta_{2h} = \frac{VB_v}{96\beta_e A^2}\left(\frac{I}{K + K_2}\right)\omega_{ch}^2\omega_{2h}$$

Note that

$$\omega_{ch} = \sqrt{\frac{K + K_2}{K}}\,\omega_c$$

$$\zeta_{ch} = \sqrt{\frac{K + K_2}{K}}\,\zeta_c$$

Thus the stability and damping of the load resonance will be slightly improved. Also, ω_{2h} and ζ_{2h} are the same as in Case II. The independence of ω_{2h} and ζ_{2h} of the hinge moment reflects the fact that this is a piston mode isolated by the load mass from hinge-moment effects.

The numerators of $\frac{x_p}{e}(s)$ and $\frac{\delta}{e}(s)$ are still given by equations (25a) and (25b), but the numerator of $\frac{P_L}{e}(s)$ has changed. The $\frac{P_L}{e}(s)$ numerator (eq. (18)) now contains the factor

$$s^4 + \frac{B_v}{m_p}s^3 + \left(\frac{K}{l^2 m_p} + \frac{K + K_2}{I}\right)s^2 + \frac{B_v(K + K_2)}{Im_p}s + \frac{KK_2}{Il^2 m_p}$$

and has the form

$$\left(s^2 + 2\zeta_{ph}\omega_{ph}s + \omega_{ph}^2\right)\left(s^2 + 2\zeta_t\omega_t s + \omega_t^2\right)$$

It is anticipated that $\omega_{ph} \approx \omega_p$ and $\omega_{ph} >> \omega_t$. Equating coefficients of s^2 and again neglecting $\frac{K + K_2}{I}$ in comparison with $\frac{K}{l^2 m_p}$ results in the expression

$$\omega_{ph}^2 = \frac{K}{l^2 m_p} = \omega_p^2$$

Then

$$\omega_{ph}^2\omega_t^2 = \frac{KK_2}{Il^2 m_p}$$

$$\omega_t^2 = \frac{K_2}{I}$$

Equating coefficients of s,

$$2\zeta_{ph}\omega_{ph} + 2\zeta_t\omega_t = \frac{B_v}{m_p}$$

Using equation (46) for ζ_{ph},

$$\zeta_t = \frac{1}{2}\sqrt{\frac{I}{K_2}}\left[\frac{B_v}{m_p} - 2\omega_{ph}\frac{B_v}{2\omega_p}\left(\frac{1}{m_p} - \frac{l^2}{I}\right)\right]$$

$$= \frac{1}{2}\sqrt{\frac{I}{K_2}}\frac{l^2 B_v}{1}$$

The factored transfer functions for this case are summarized in table 1. The simplified models of equations (31) and (25) may be obtained by setting m_p, B_v, or K_2 equal to zero. Thus the subscript h was eliminated from the parameters in table 1.

APPENDIX C

CONTROL: A DIGITAL PROGRAM FOR THE DETERMINATION OF TRANSFER FUNCTIONS, ROOT LOCI, AND FREQUENCY RESPONSES

The CONTROL digital program was used to generate the transfer functions, root loci, and frequency responses of the linear model. The program uses the state variable formulation of the linear equations of motion:

$$\dot{\underline{x}} = F\underline{x} + B\underline{u} \tag{34}$$

where

$\underline{x}$ is the $n \times 1$ vector

F is the $n \times n$ matrix

B is the $n \times m$ matrix

$\underline{u}$ is the $m \times 1$ vector

n is the dimension of the system,

m is the number of inputs into the system.

From the closed-loop system matrix of equation (32), $n = 7$ and $m = 2$.

An $m \times n$ feedback matrix, G, is defined as

$$\underline{u} = \underline{u}_c + G\underline{x}$$

where $\underline{u}_c$ is a command input. Then equation (34) becomes

$$\dot{\underline{x}} = \left[F + BG\right]\underline{x} + B\underline{u}_c \tag{35}$$

The eigenvalues of the matrix F in equation (34) give the roots of the characteristic equation of the open-loop system, and the eigenvalues of the matrix $\left[F + BG\right]$ in equation (35) give the roots of the characteristic equation of the closed-loop system. The CONTROL program uses the IBM Share program QREIG (i.e., the QR algorithm) to find the eigenvalues. Setting

$$G = aG_1 + bG_2$$

where G_1 and G_2 are $m \times n$ matrices and $a, b = 0, 1, 2. \ldots .$, the eigenvalues

of $[F + BG]$ yield root loci for the two feedback quantities associated with the matrices G_1 and G_2.

REFERENCES

1. Morse, Allen C.: Electrohydraulic Servomechanisms. McGraw-Hill Book Co., Inc., 1963.

2. Collette, J. G. Rolland: Analysis and Design of Space Vehicle Flight Control Systems. Vol. XI - Component Dynamics. General Dynamics Corp. (NASA CR-830), 1967.

3. Greensite, Arthur L.: Analysis and Design of Space Vehicle Flight Control Systems. Vol. VII - Attitude Control During Launch. General Dynamics Corp. (NASA CR-826), 1967.

4. Anon.: Aircraft Load Alleviation and Mode Stabilization (LAMS). AFFDL-TR-68-158, Air Force Flight Dynamics Lab., Wright-Patterson Air Force Base, Dec. 1968.

5. Peters, R. A.; and Graham, Dunstan, eds.: Aircraft Hydraulic Servomechanisms. Tech. Rep. No. 129-2, Systems Technology, Inc., March 1969.

6. Merritt, Herbert E.: Hydraulic Control Systems. John Wiley & Sons, Inc., 1967.

7. Lewis, Ernest E.; and Stern, Hansjoerg: Design of Hydraulic Control Systems. McGraw-Hill Book Co., Inc., 1962.

8. Thayer, W. J.: Transfer Functions for Moog Servovalves. Tech. Bull. No. 103, Moog Servocontrols, Inc., Jan. 1965.

9. Etkin, Bernard: Dynamics of Flight—Stability and Control. John Wiley & Sons, Inc., 1959.

10. D' Azzo, John J.; and Houpis, Constantine H.: Feedback Control System Analysis and Synthesis. McGraw-Hill Book Co., Inc., 1966.

11. Clark, Daniel C.; and Kroll, John: General Purpose Airborne Simulator—Conceptual Design Report. Cornell Aeronautical Laboratory, Inc. (NASA CR-544), 1966.

TABLE 1.–APPROXIMATE OPEN-LOOP LITERAL TRANSFER FUNCTIONS

$$\frac{x_p}{e}(s) = \frac{1}{\Delta(s)} \frac{K_s K_q}{12A} \left(\frac{s^2}{\omega_s^2} + 1 \right)$$

$$\frac{\delta}{e}(s) = \frac{1}{\Delta(s)} \frac{K K_s K_q}{12A\ell (K + K_2)}$$

$$\frac{P_L}{e}(s) = \frac{1}{\Delta(s)} \frac{I K K_s K_q}{12A^2 \ell^2 (K + K_2)} \left(\frac{s^2}{\omega_p^2} + \frac{2\zeta_p}{\omega_p} s + 1 \right) \left(s^2 + 2\zeta_t \omega_t s + \omega_t^2 \right)$$

$$\Delta(s) = (s + p_3)(\tau_s s + 1) \left(\frac{s^2}{\omega_c^2} + \frac{2\zeta_c}{\omega_c} s + 1 \right) \left(\frac{s^2}{\omega_2^2} + \frac{2\zeta_2}{\omega_2} s + 1 \right)$$

where

$$p_3 = \frac{K K_2 K_c}{12A^2 \ell^2 (K + K_2)}$$

$$\omega_s^2 = \frac{K + K_2}{I}$$

$$\omega_h^2 = \frac{48 \beta_e A^2 \ell^2 (K + K_2)}{IVK}$$

$$\frac{1}{\omega_c^2} = \frac{1}{\omega_s^2} + \frac{1}{\omega_h^2}$$

$$\omega_t^2 = \frac{K_2}{I}$$

$$\zeta_c = \frac{I K_c}{24 A^2 \ell^2} \omega_c$$

$$\zeta_t = \frac{\ell^2 B_v}{2I} \sqrt{\frac{I}{K_2}}$$

$$\omega_p^2 = \frac{K}{\ell^2 m_p}$$

$$\zeta_p = \frac{B_v}{2\omega_p} \left(\frac{1}{m_p} - \frac{\ell^2}{I} \right)$$

$$\omega_2^2 = \frac{VK + 48 \beta_e A^2 \ell^2}{IV \ell^2 m_p}$$

$$\zeta_2 = \frac{V B_v}{96 \beta_e A^2} \left(\frac{I}{K + K_2} \right) \omega_c^2 \omega_2$$

TABLE 2.–RUDDER MODEL CONSTANTS

I	1.8 slug-ft^2
m_p	0.166 slug
K	10,800 ft-lb/rad
ℓ	0.158 ft
V	5 in^3
A	1.0 in^2
β_e	50,000 psi
K_v	3.05 in^3-sec^{-1}/in. $\sqrt{\text{psi}}$
K_q	167 in^3-sec^{-1}/in.
K_1	940 ft-lb/rad
K_2	1340 ft-lb/rad
K_s	0.003 in/V
τ_s	0.0025 sec
$\lvert\delta_r\rvert$	$< 30°$
$\lvert\dot{\delta}_r\rvert$	< 109 deg/sec
	Nonlinear model
B_v	500 lb/ft-sec^{-1}
B_c	40 lb
K_c	0.0278 in^3-sec^{-1}/psi
	Linear model
B_v	2000 lb/ft-sec^{-1}
B_c	0
K_c	0.000084 in^3-sec^{-1}/psi
$x_{s_{max}}$	0.003 in.

TABLE 3.–COMPARISON OF APPROXIMATE LITERAL FACTORS AND EXACT FACTORS

Approximate literal factors		Case I		Case II		Case III	
		Exact	Approximate	Exact	Approximate	Exact	Approximate
ω_s	$\sqrt{\frac{K + K_2}{I}}$	77.46	77.46	77.46	77.46	82.12	82.12
ω_h	$\sqrt{\frac{48\beta_e A^2 l^2 (K + K_2)}{IVK}}$	-----	-----	-----	81.59	-----	86.5
ω_c	$\frac{1}{\omega_c^2} = \frac{1}{\omega_s^2} + \frac{1}{\omega_h^2}$	56.18	56.18	56.7	56.18	63.0	59.57
ζ_c	$\frac{K_c I}{24A^2 l^2}\omega_c$	.0139	.0139	.068	.0139	.059	.0148
p_3	$\frac{KK_2K_c}{12A^2 l^2 (K + K_2)}$	-----	-----	-----	-----	.297	.331
ω_2	$\sqrt{\frac{VK + 48\beta_e A^2 l^2}{IVl^2 m_p}}$	-----	-----	2330	1747	2330	1747
ζ_2	$\frac{VB_v}{96\beta_e A^2}\left(\frac{I}{K + K_2}\right)\omega_c^2\omega_2$	-----	-----	2.58	1.91	2.58	1.91
ω_p	$\sqrt{\frac{K}{l^2 m_p}}$	-----	-----	1490	1614	1490	1614
ζ_p	$\frac{B_v}{2\omega_p}\left(\frac{1}{m_p} - \frac{l^2}{I}\right)$	-----	-----	4.02	3.12	4.02	3.12
ω_t	$\sqrt{\frac{K_2}{I}}$	-----	-----	-----	-----	29.4	27.28
ζ_t	$\frac{l^2 B_v}{2I}\sqrt{\frac{I}{K_2}}$	-----	-----	-----	-----	.54	.508
z_1	$\frac{l^2 B_v}{I}$	-----	-----	32.62	21.14	-----	-----
K_β	$\frac{K_1}{K + K_2}$	-----	-----	-----	-----	.0825	.0775

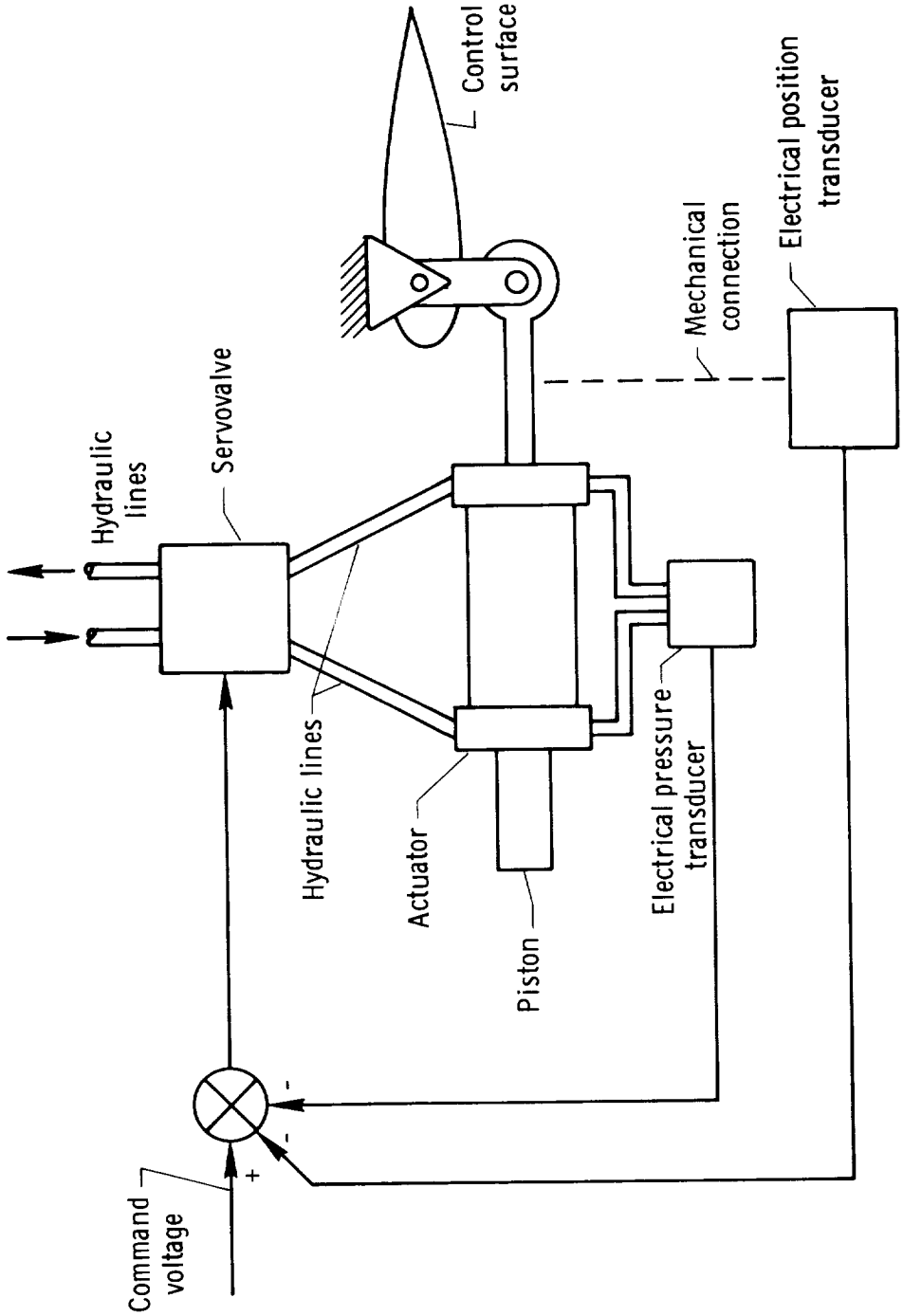

(a) Functional diagram.

Figure 1. Aircraft control-surface servo model.

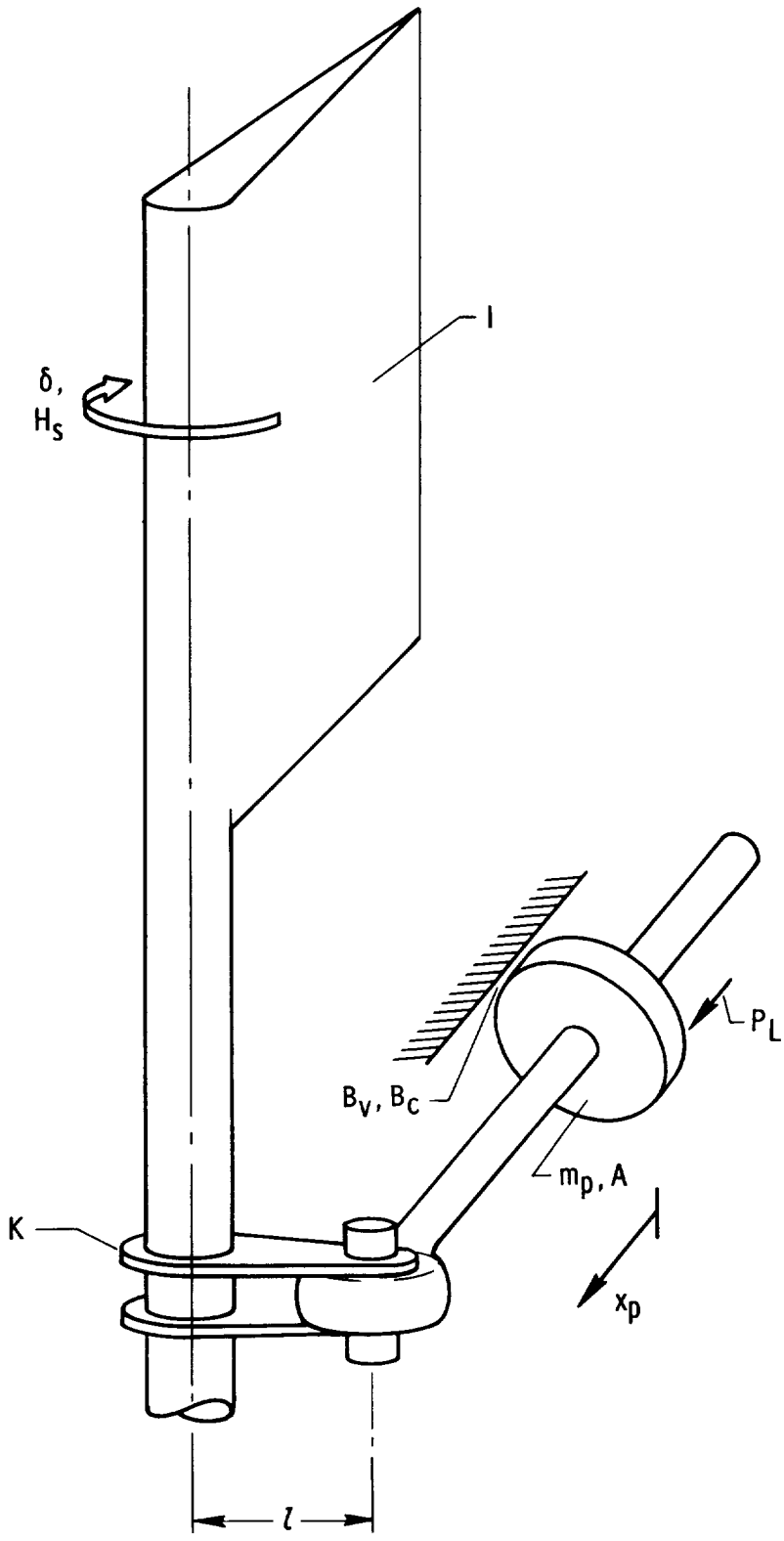

(b) Mechanical diagram.

Figure 1. Continued.

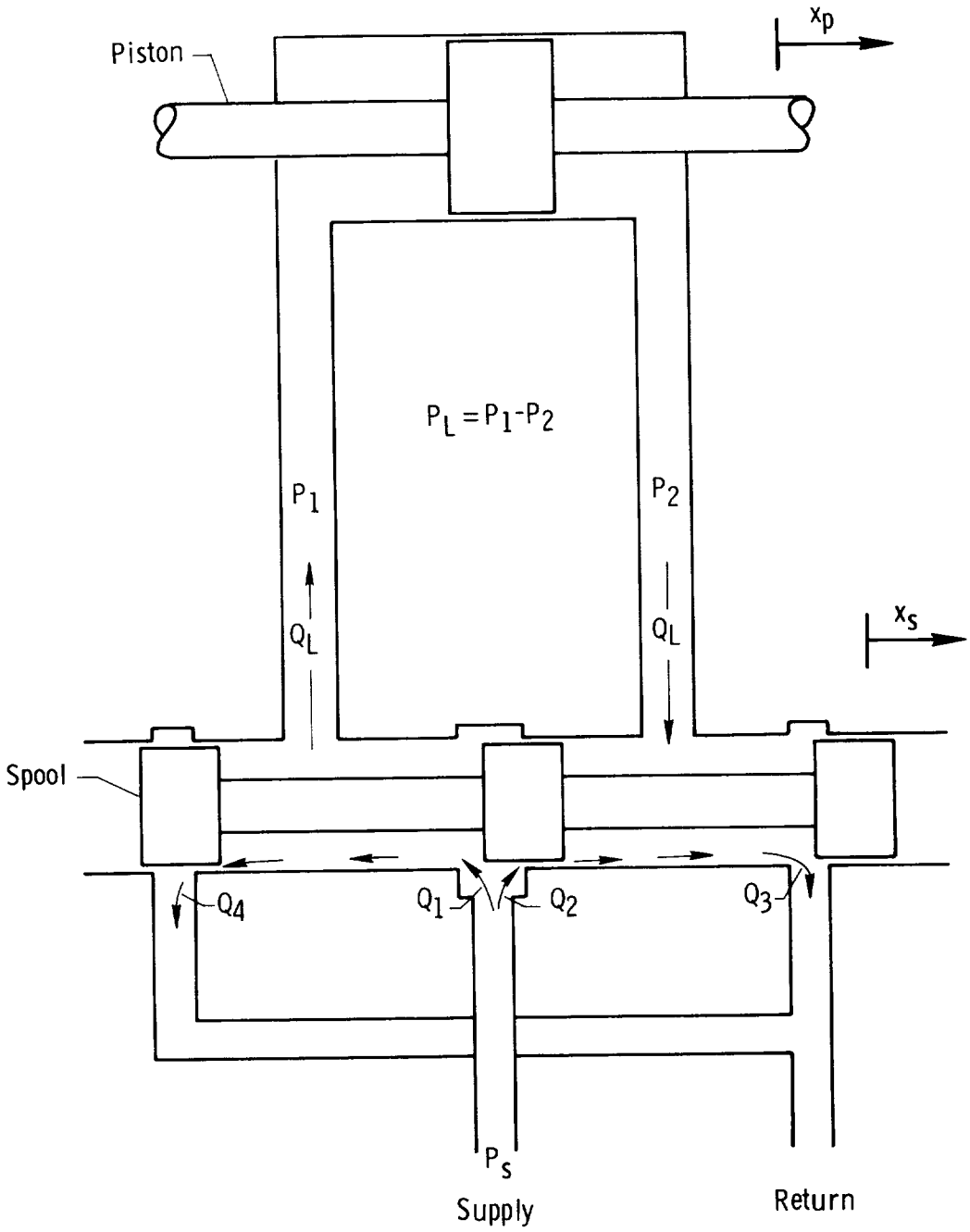

(c) Hydraulic diagram showing second stage of the servo valve (spool valve) and the actuator piston.

Figure 1. Concluded.

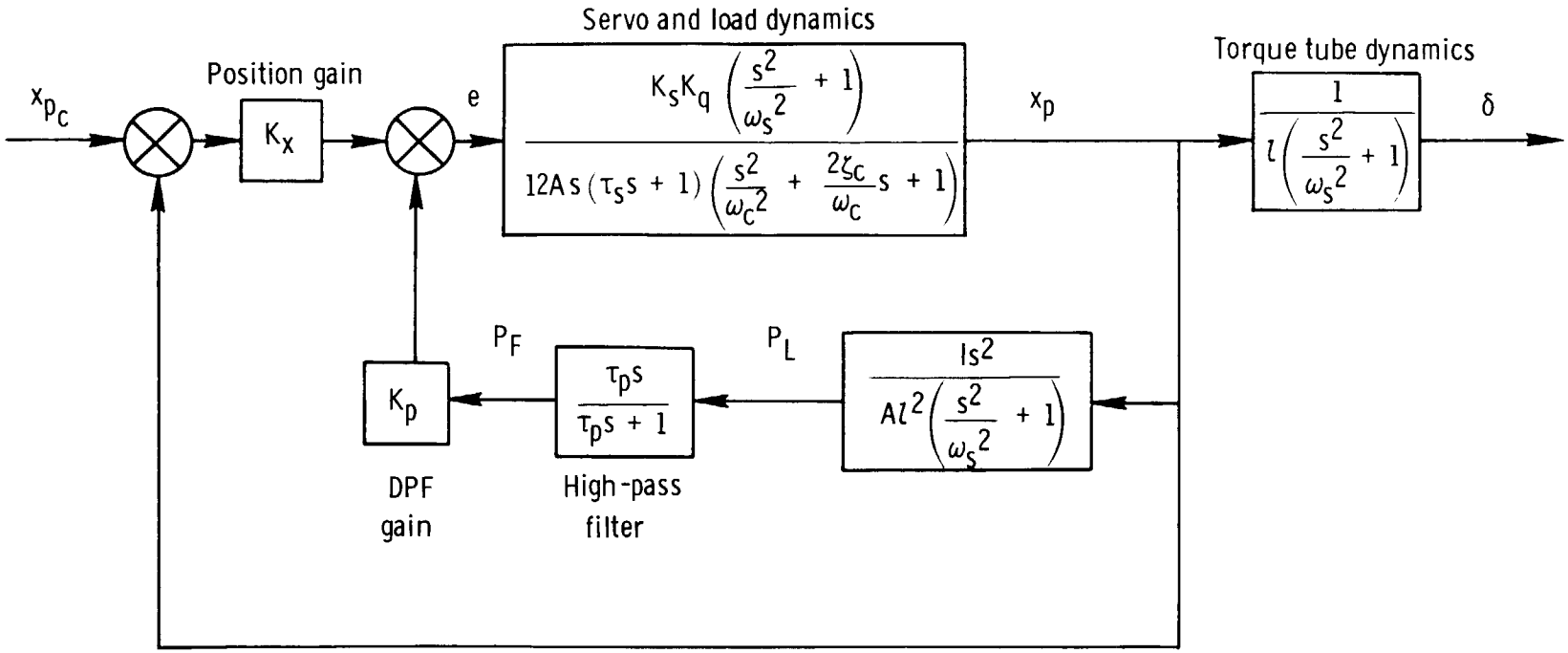

Figure 2. Closed-loop block diagram of an aircraft control-surface control system with position feedback and dynamic pressure feedback. Case I; $m_p = K_2 = \beta_v = 0$.

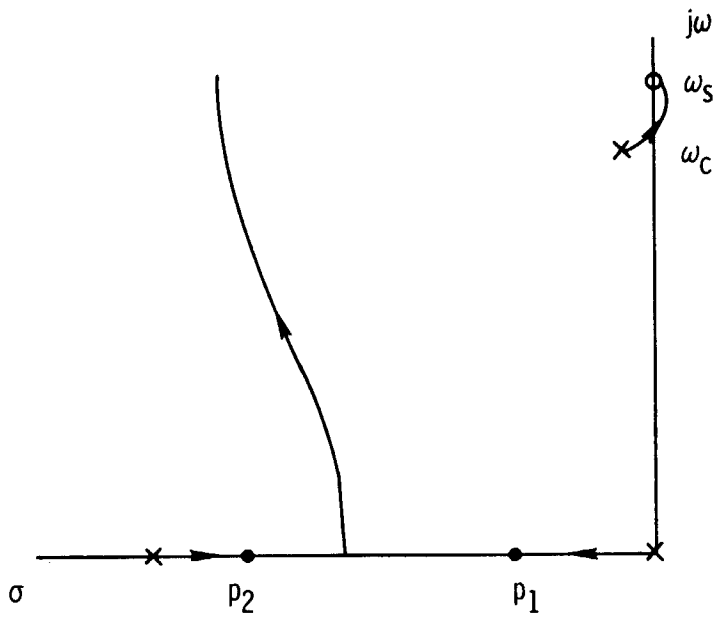

(a) Position loop closure only.

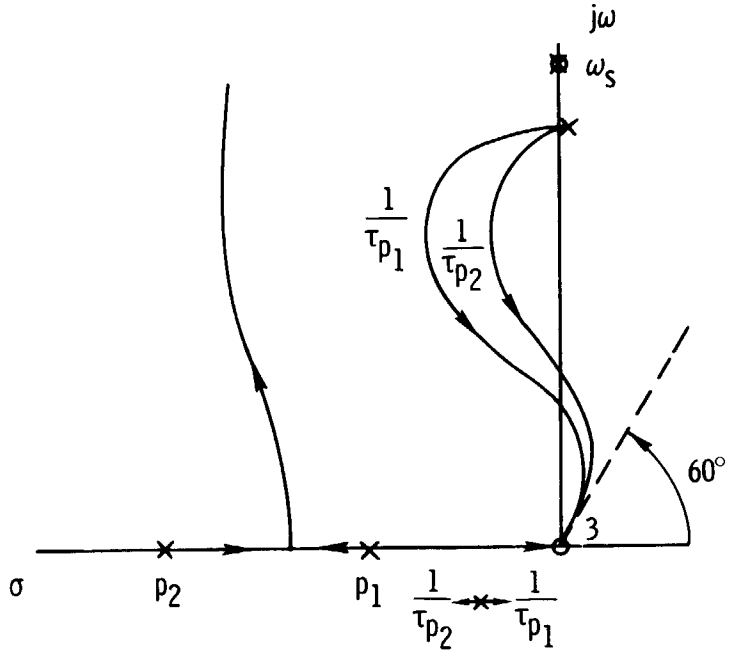

(b) Pressure loop closure following position loop closure $\left(\frac{1}{\tau_{p_1}} < \frac{1}{\tau_{p_2}}\right)$.

Figure 3. Root loci for position and pressure loop closures for Case I. $m_p = K_2 = \beta_v = 0$.

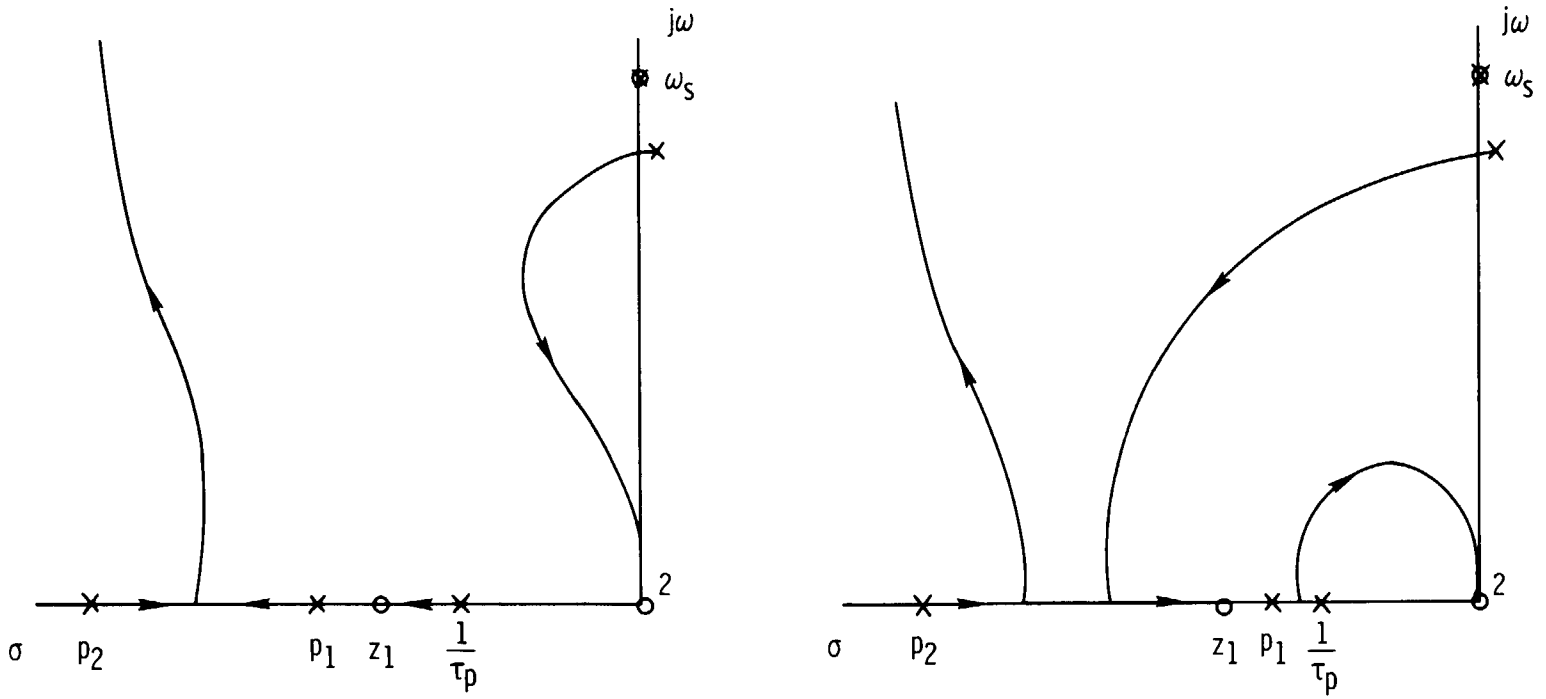

(a) $p_1 > z_1$.

(b) $p_1 < z_1$.

Figure 4. Root loci of pressure loop closure following position loop closure for Case II. $K_2 = 0$.

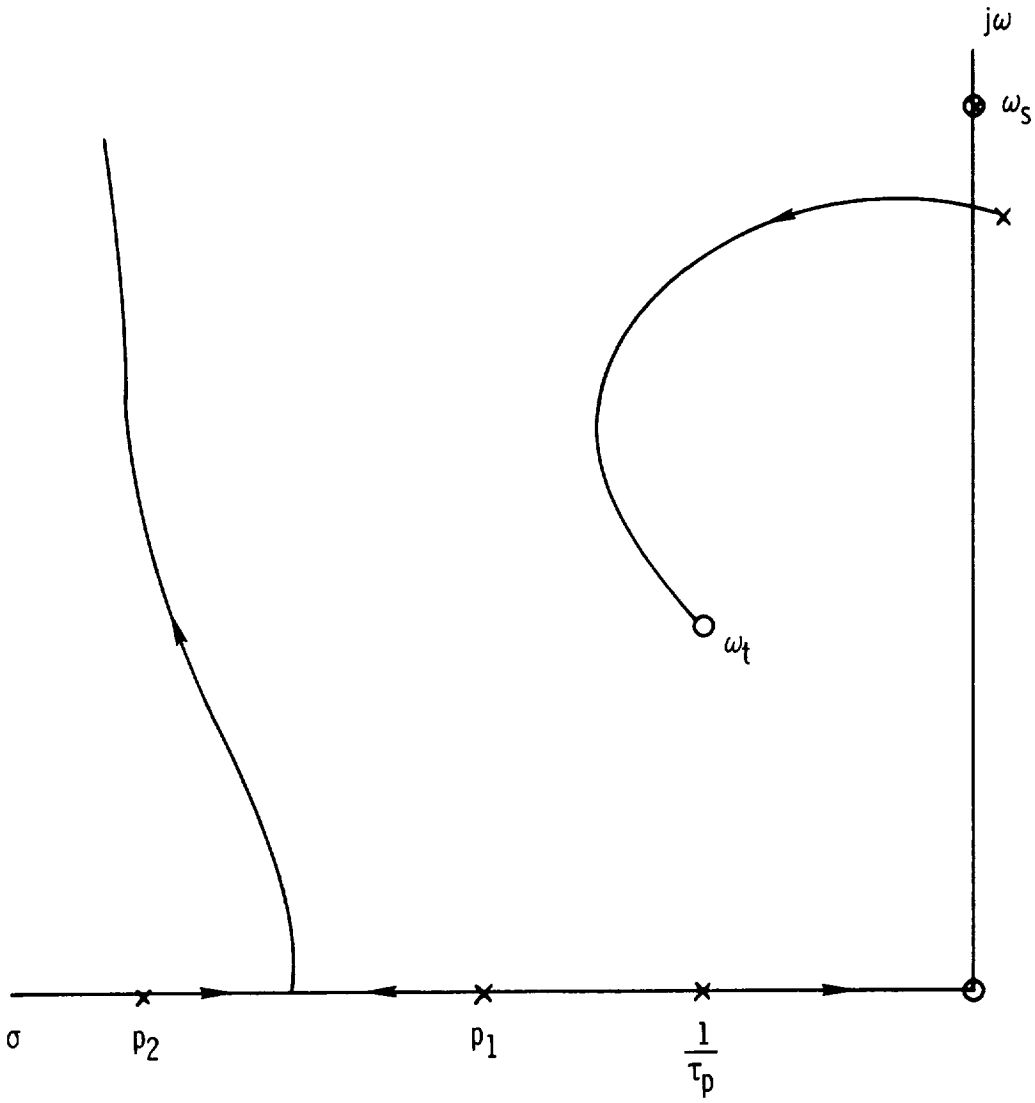

Figure 5. Root loci for pressure loop closure following position loop closure for Case III. K_x = 1090 V/ft; $\frac{1}{\tau_p}$ = 16.6 rad/sec.

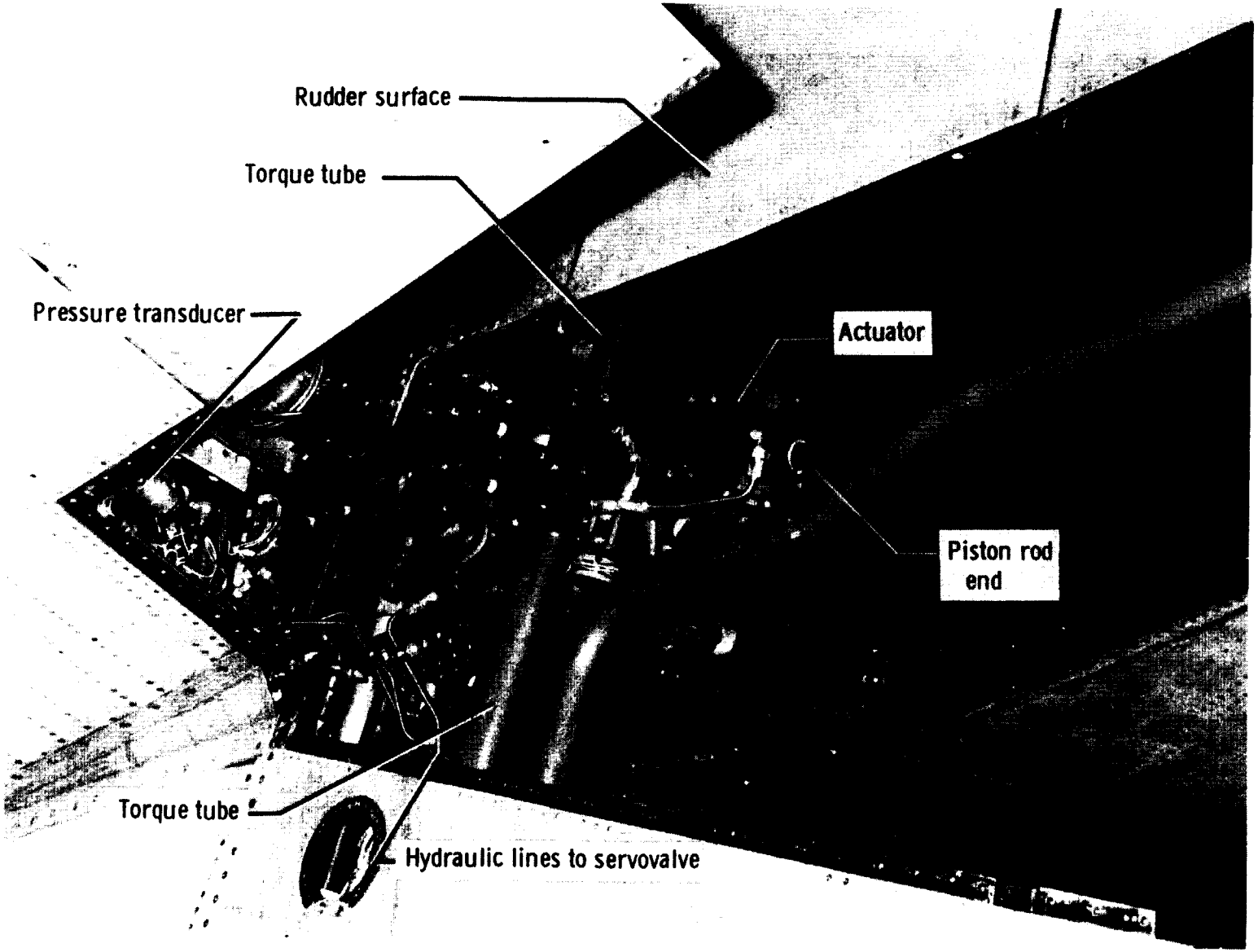

Figure 6. Rudder surface and electrohydraulic actuator. E-19830

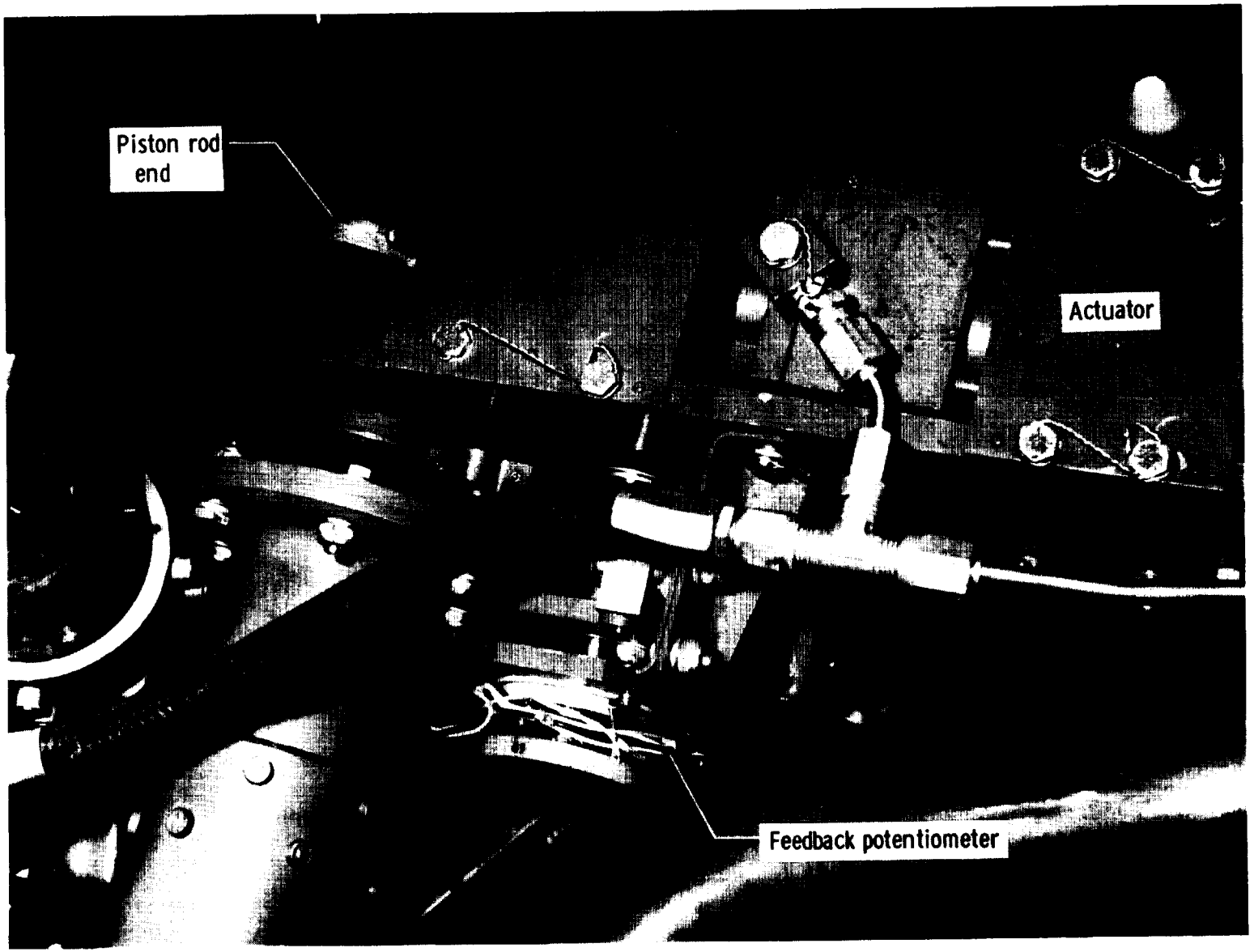

Figure 7. Closeup of rudder electrohydraulic actuator. E-19831

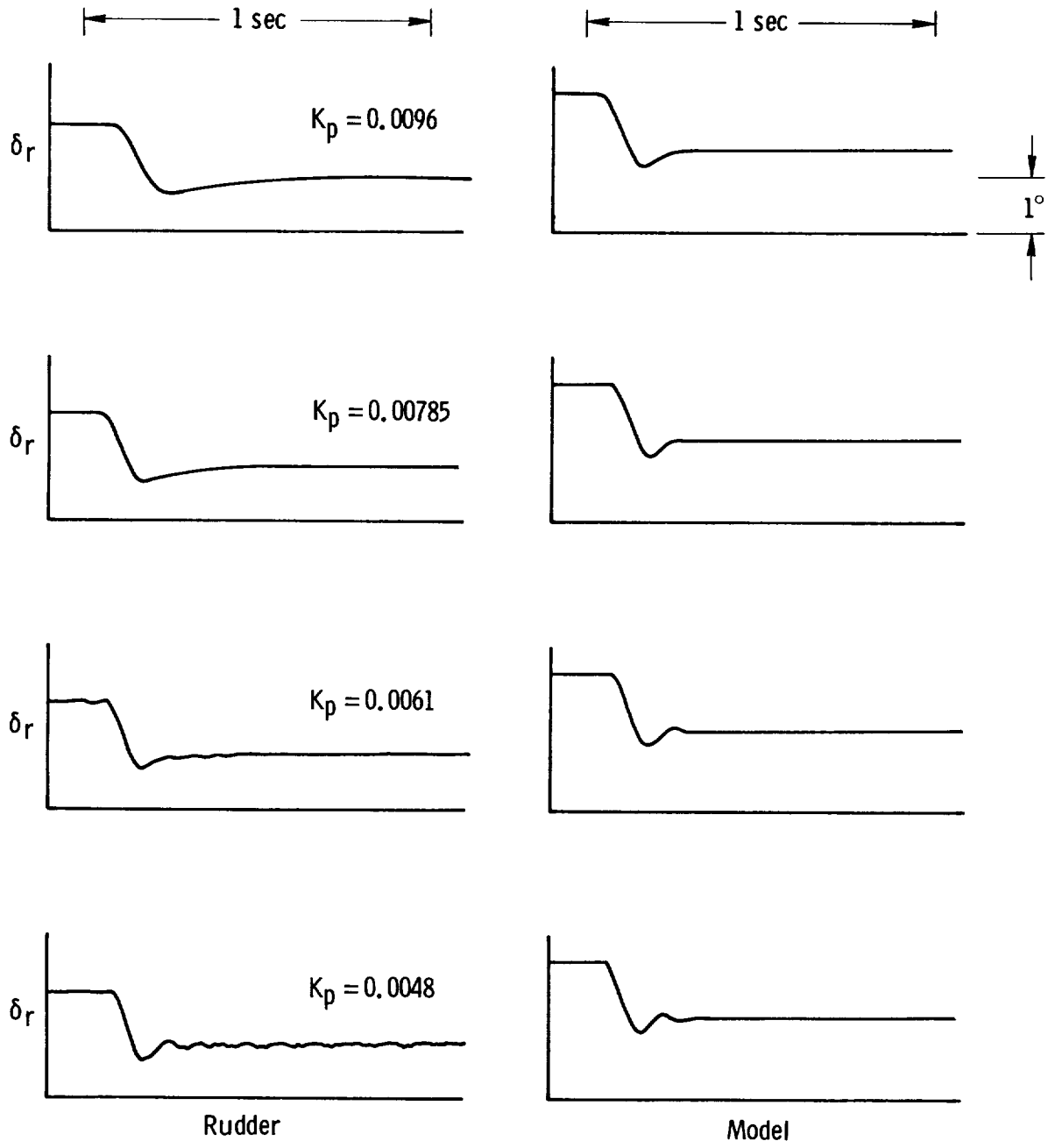

(a) $\frac{1}{\tau_p} = 8.3$ rad/sec.

Figure 8. Rudder and model step response as a function of K_p and τ_p. $\delta_{r_c} = 1°$.

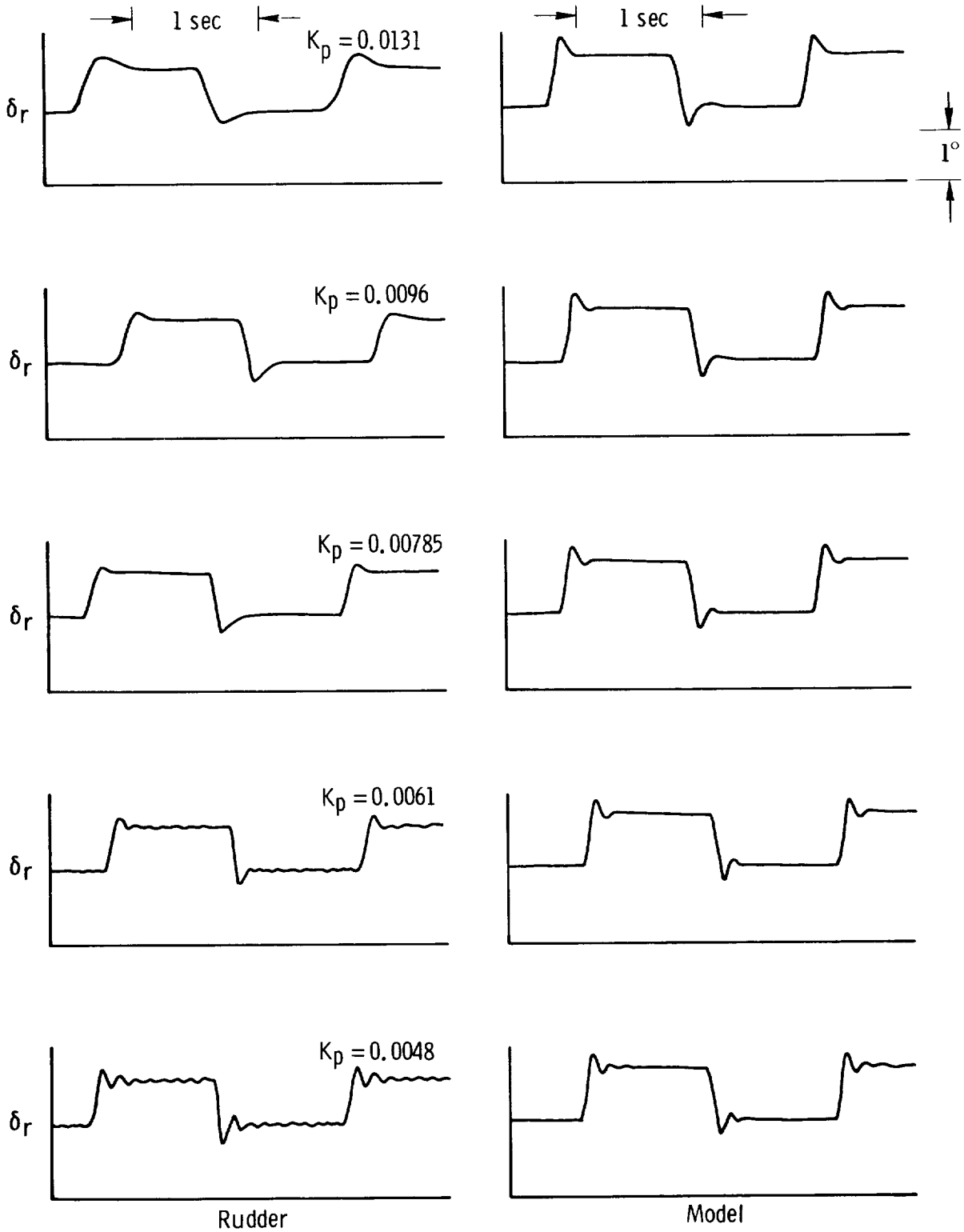

(b) $\frac{1}{\tau_p} = 16.6$ rad/sec.

Figure 8. Continued.

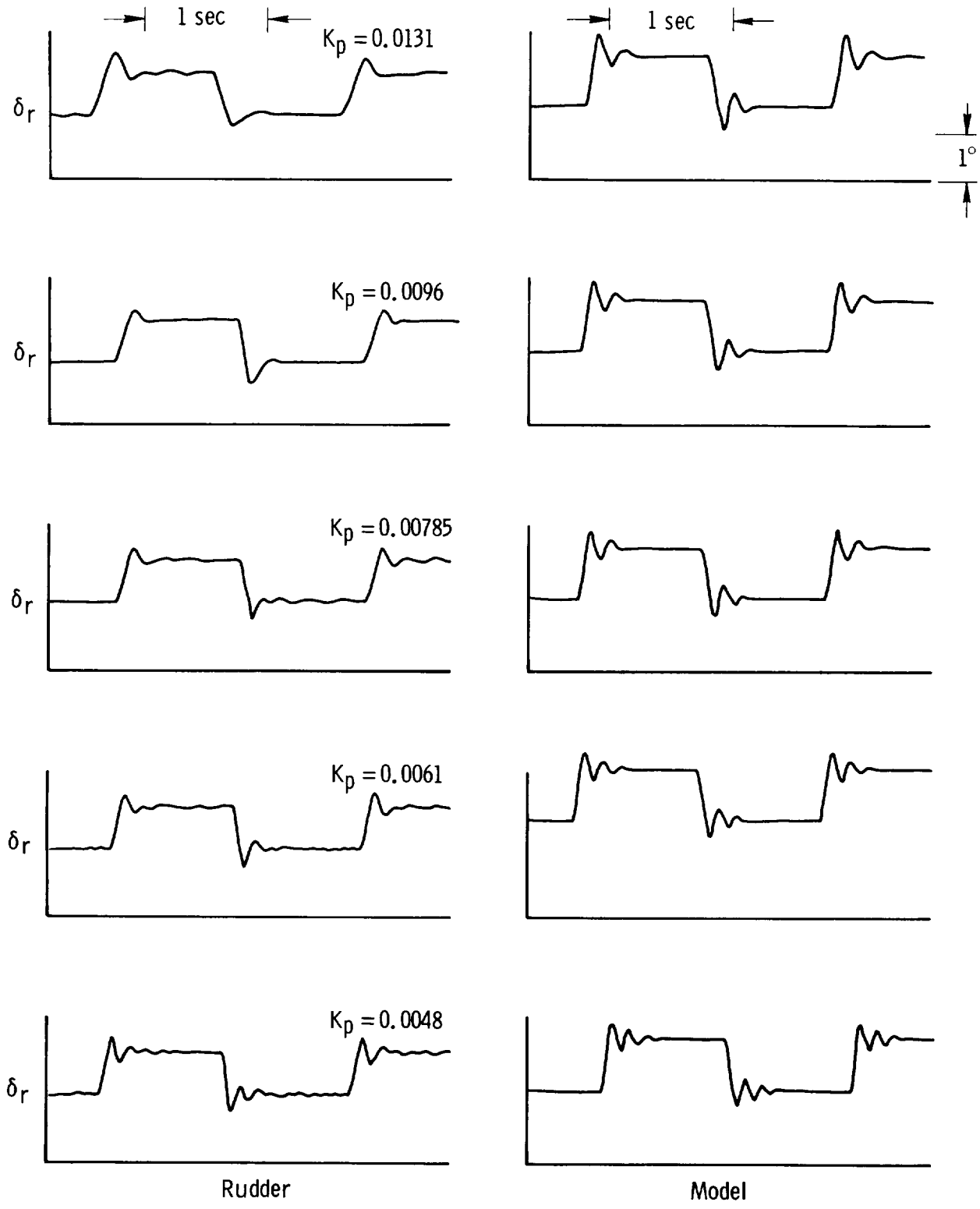

(c) $\frac{1}{\tau_p} = 33.2$ rad/sec.

Figure 8. Concluded.

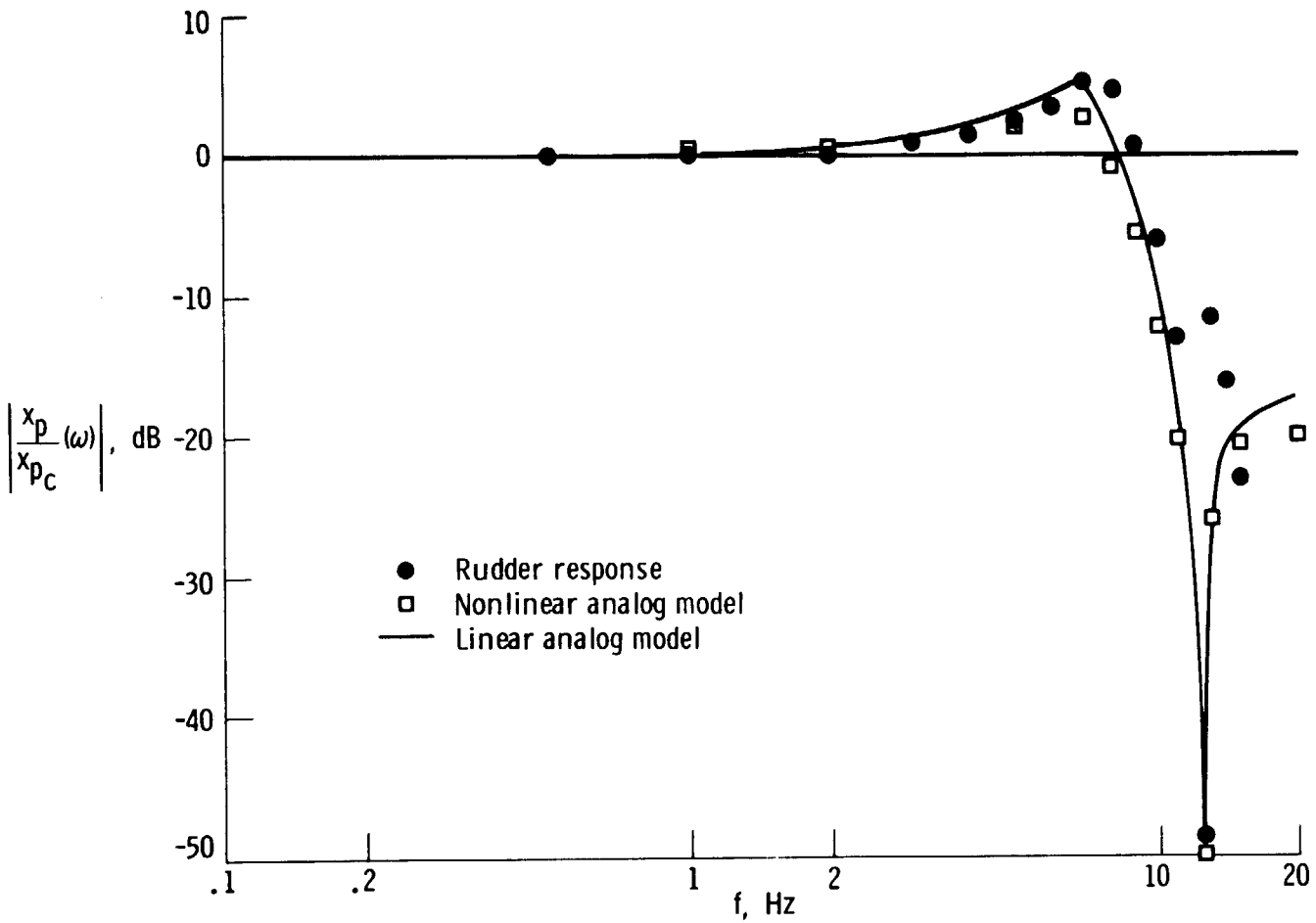

(a) Magnitude.

Figure 9. Ground test frequency response of the rudder, the nonlinear model, and the linear model. $\delta_{rc} = 1.0°$, peak to peak; $K_x = 1090$ V/ft; $K_p = 0.0048$ V/psi; $\frac{1}{\tau_p} = 16.6$ rad/sec.

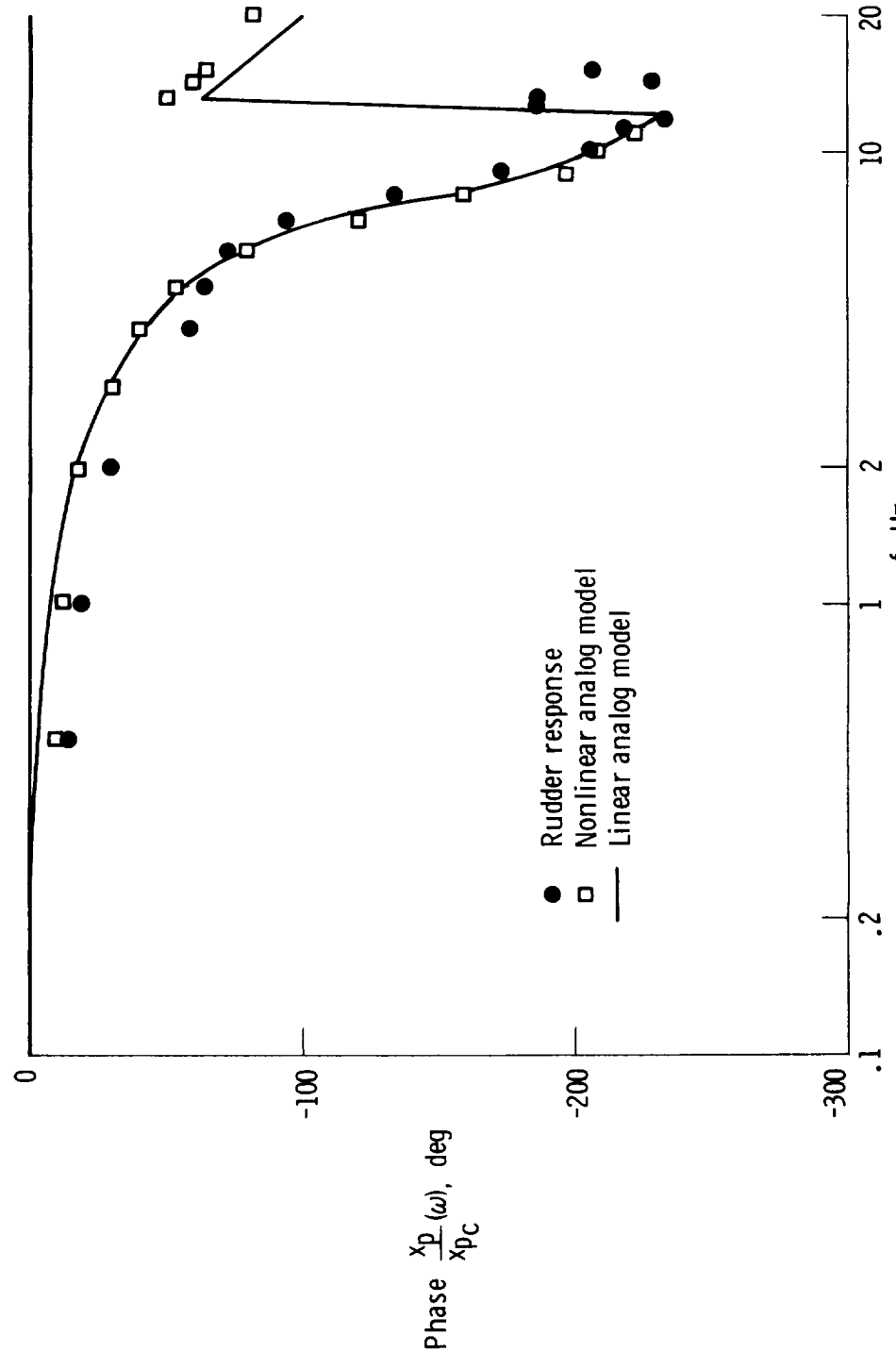

(b) Phase angle.

Figure 9. Concluded.

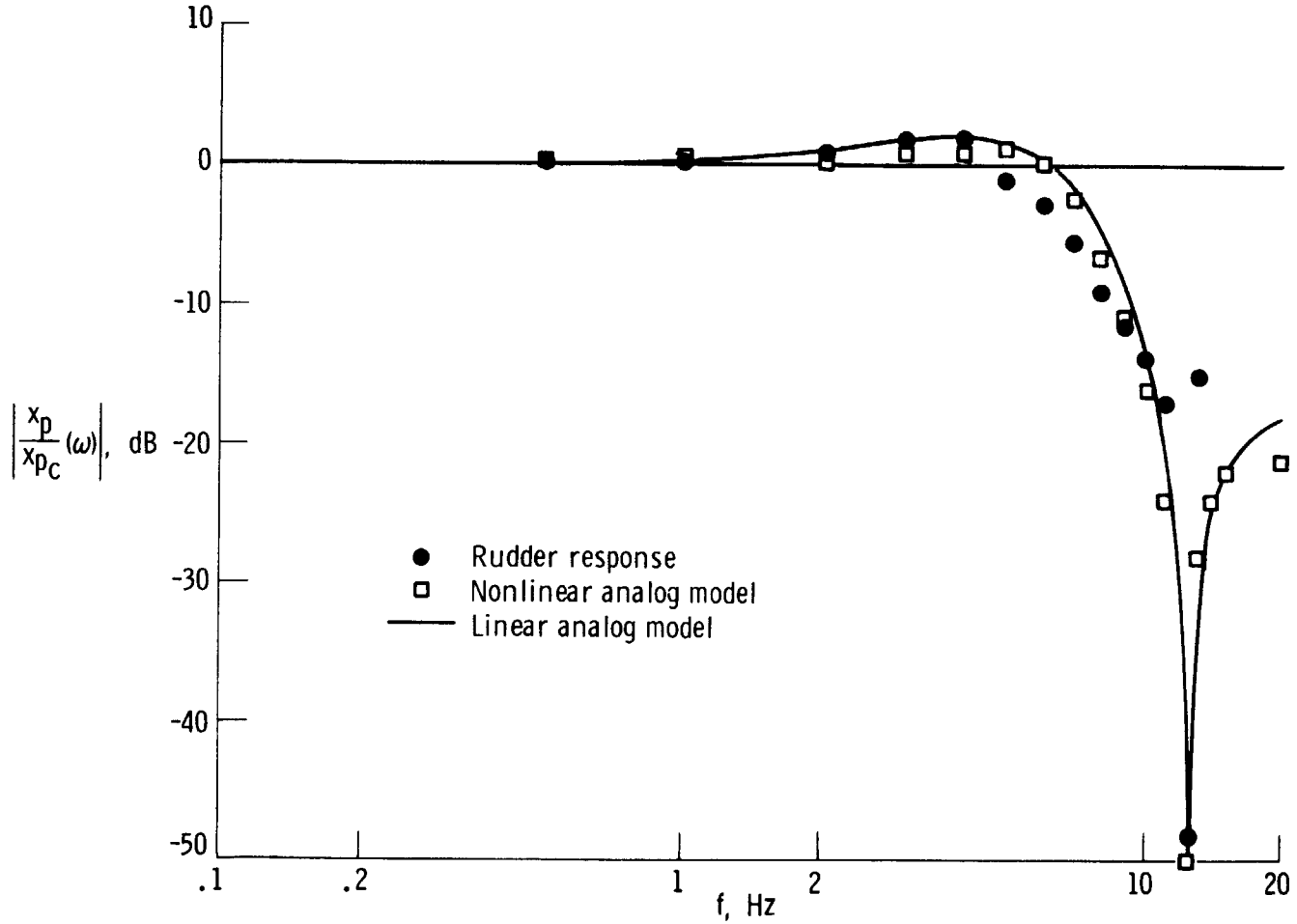

(a) Magnitude.

Figure 10. Ground test frequency response. $\delta_{r_c} = 1.0°$, peak to peak; $K_x = 1090$ V/ft; $K_p = 0.00785$ V/psi; $\frac{1}{\tau_p} = 8.3$ rad/sec.

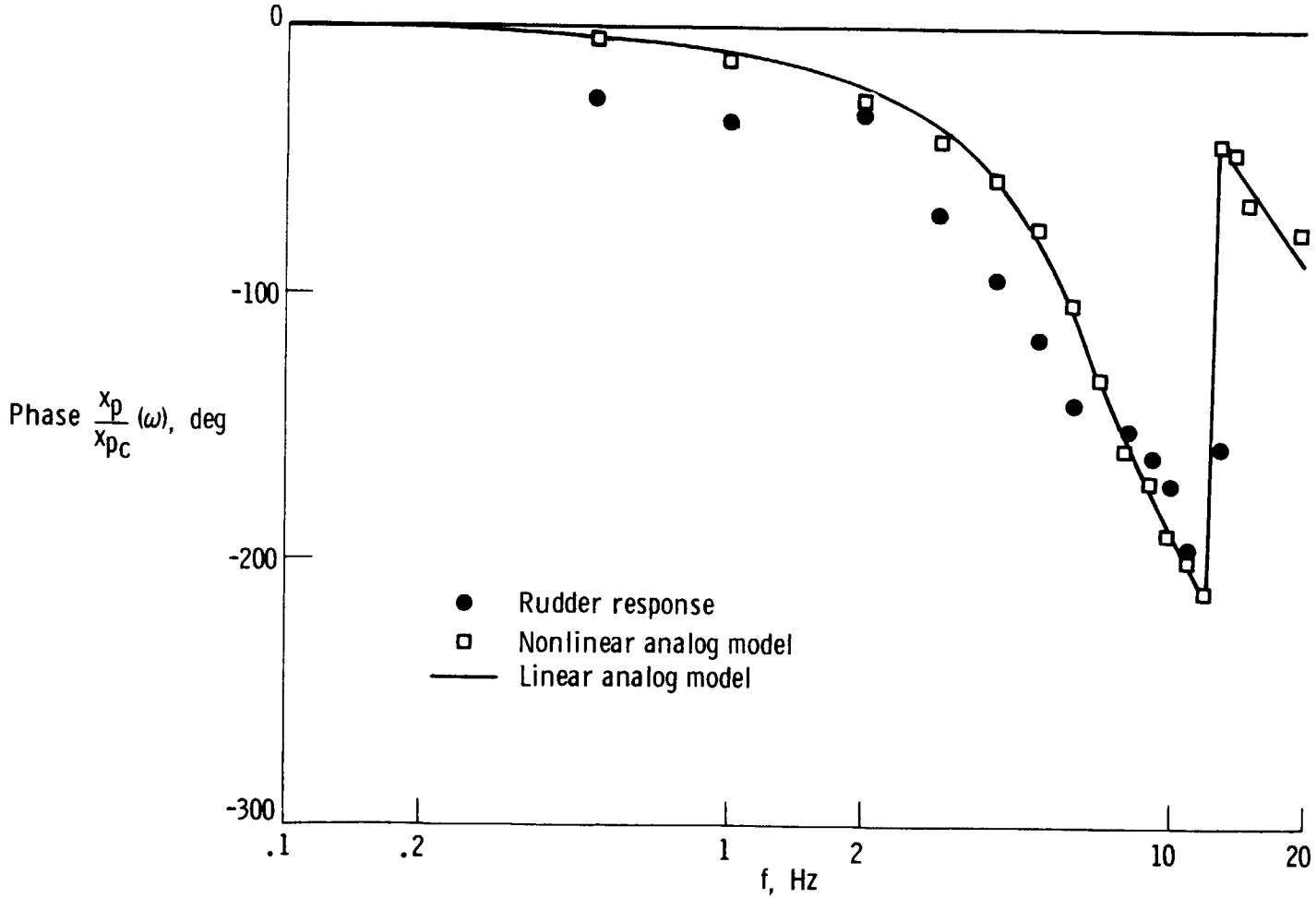

(b) Phase angle.

Figure 10. Concluded.

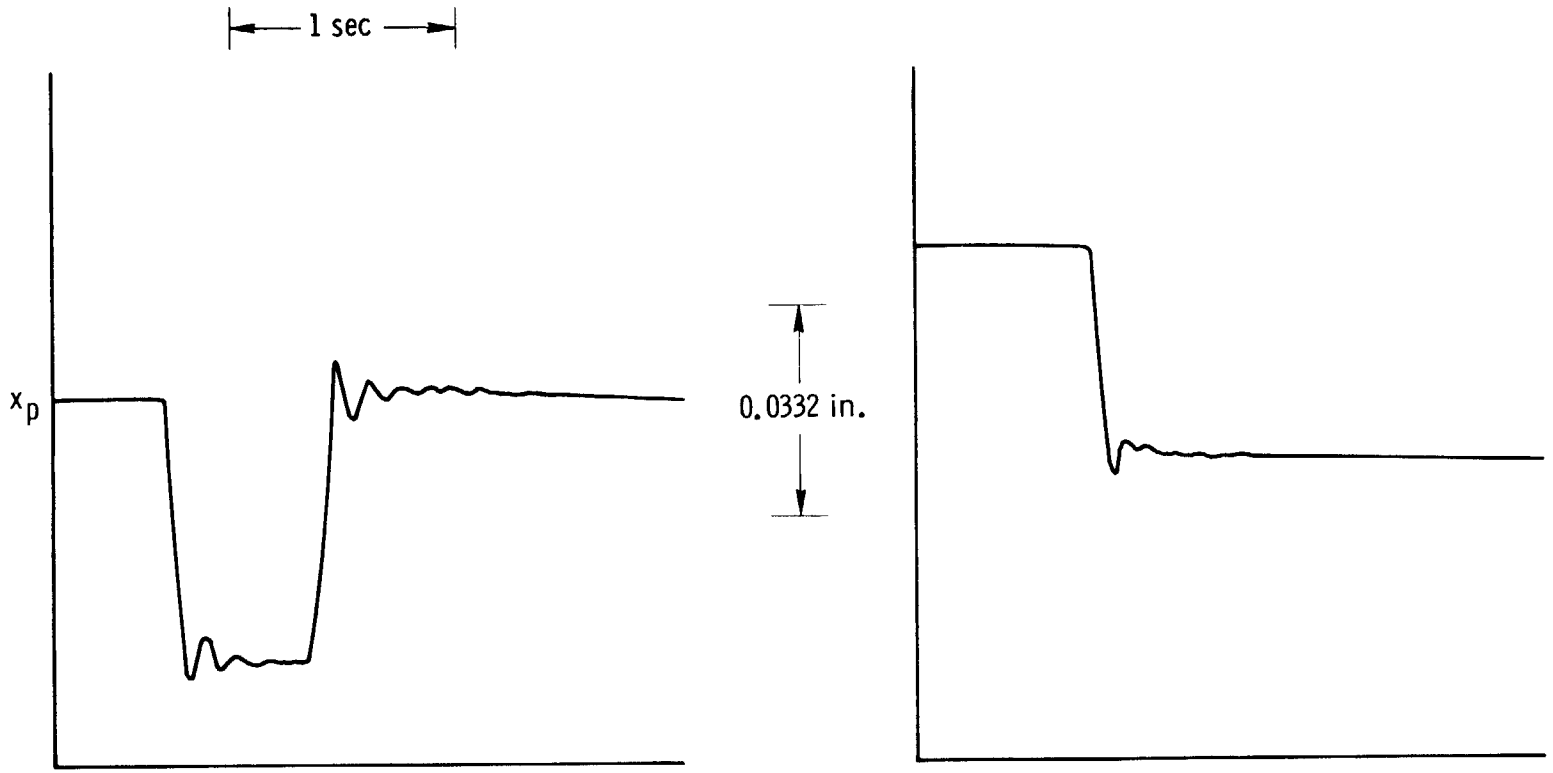

(a) Ground test.

(b) Flight test.

Figure 11. Rudder step response in ground and flight tests. K_x = 1090 V/ft; K_p = 0.0048 V/psi; $\frac{1}{\tau_p}$ = 16.6 rad/sec.

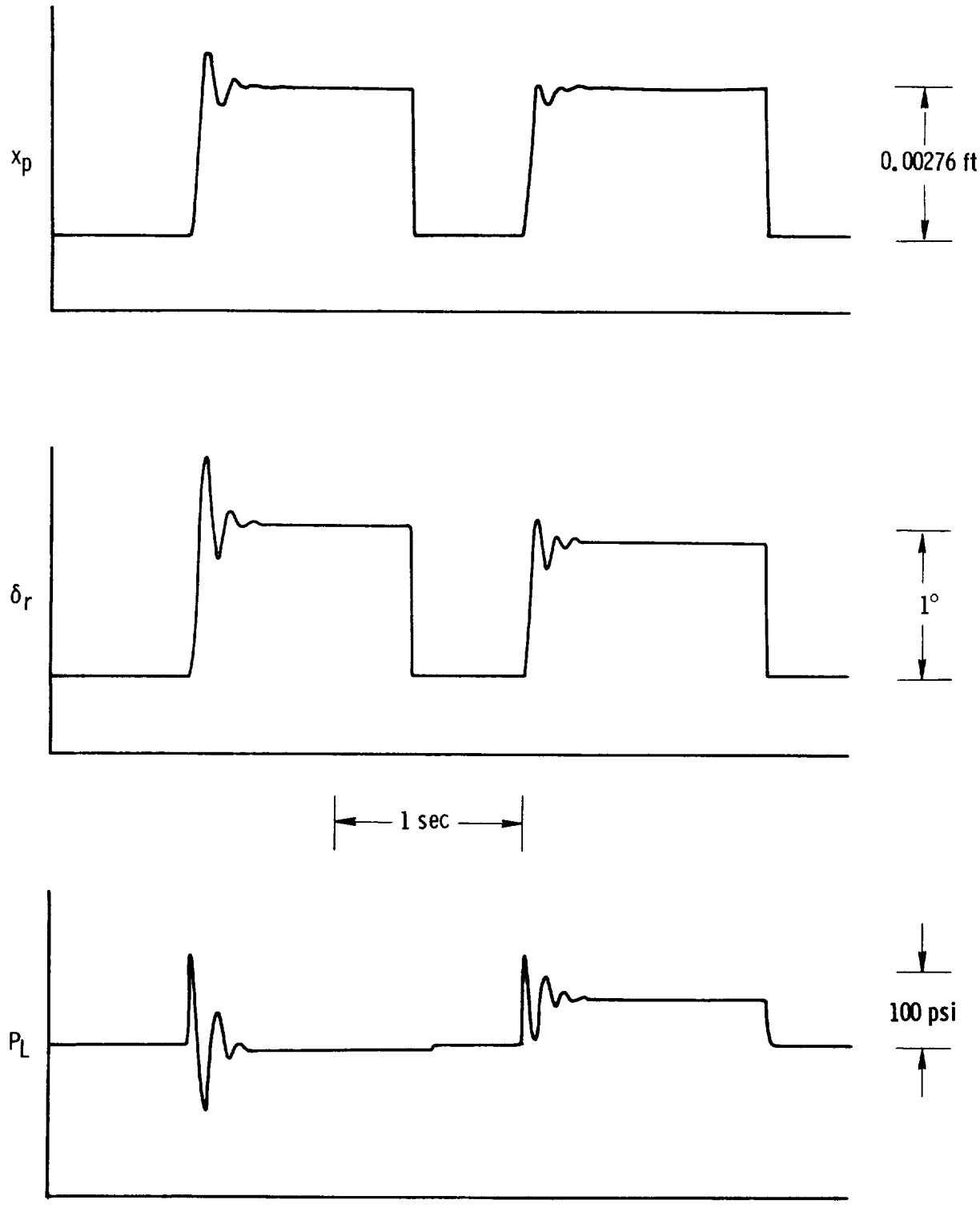

(a) Simulated ground test. (b) Simulated flight test.

Figure 12. Nonlinear model step response in simulated ground and flight tests. K_x = 1090 V/ft; K_p = 0.0048 V/psi; $\frac{1}{\tau_p}$ = 16.6 rad/sec.

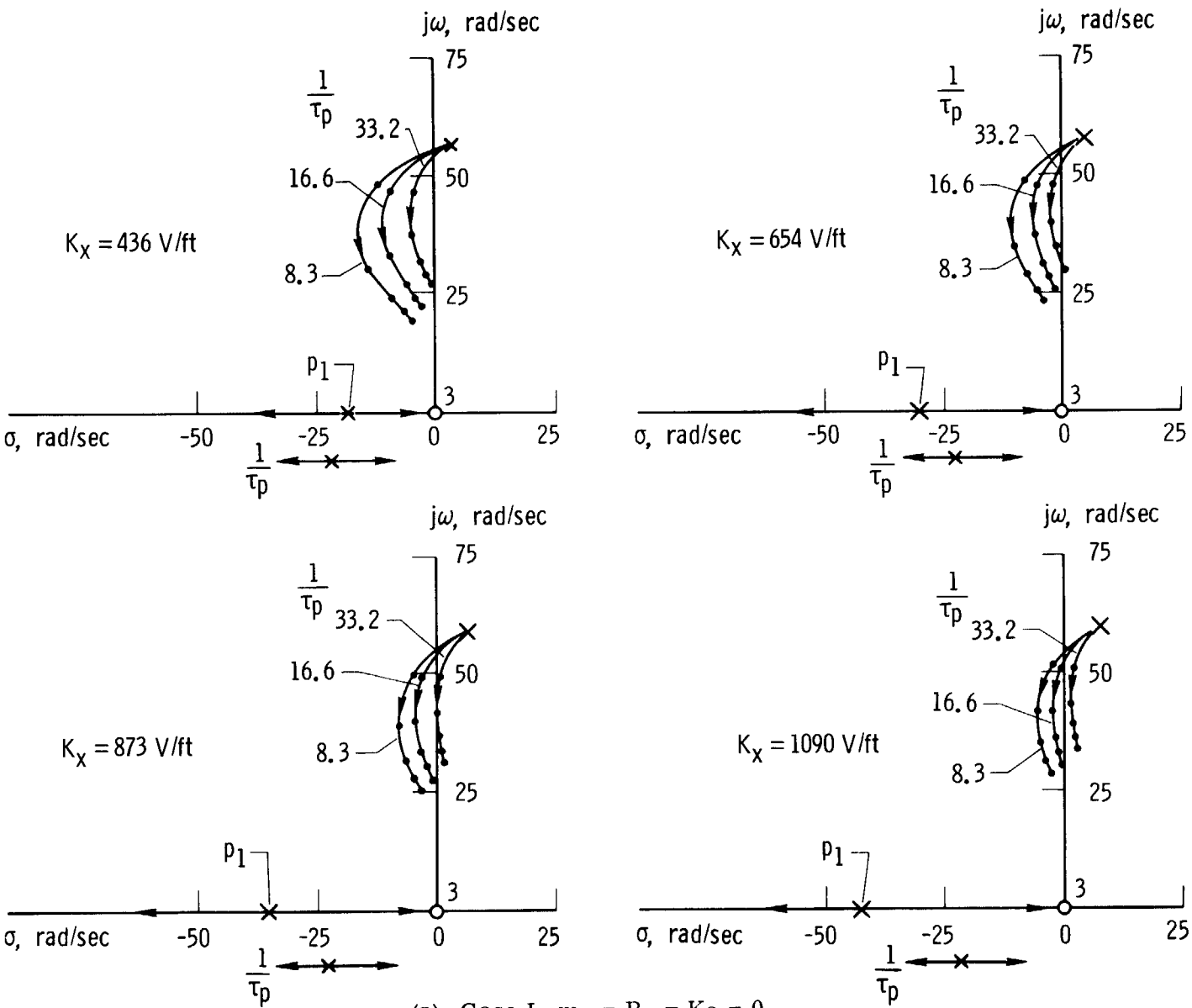

(a) Case I, $m_p = B_v = K_2 = 0$.

Figure 13. Linear model pressure loop closure root loci as a function of K_x, K_p, and τ_p. $\Delta K_p = 0.00348$ V/psi.

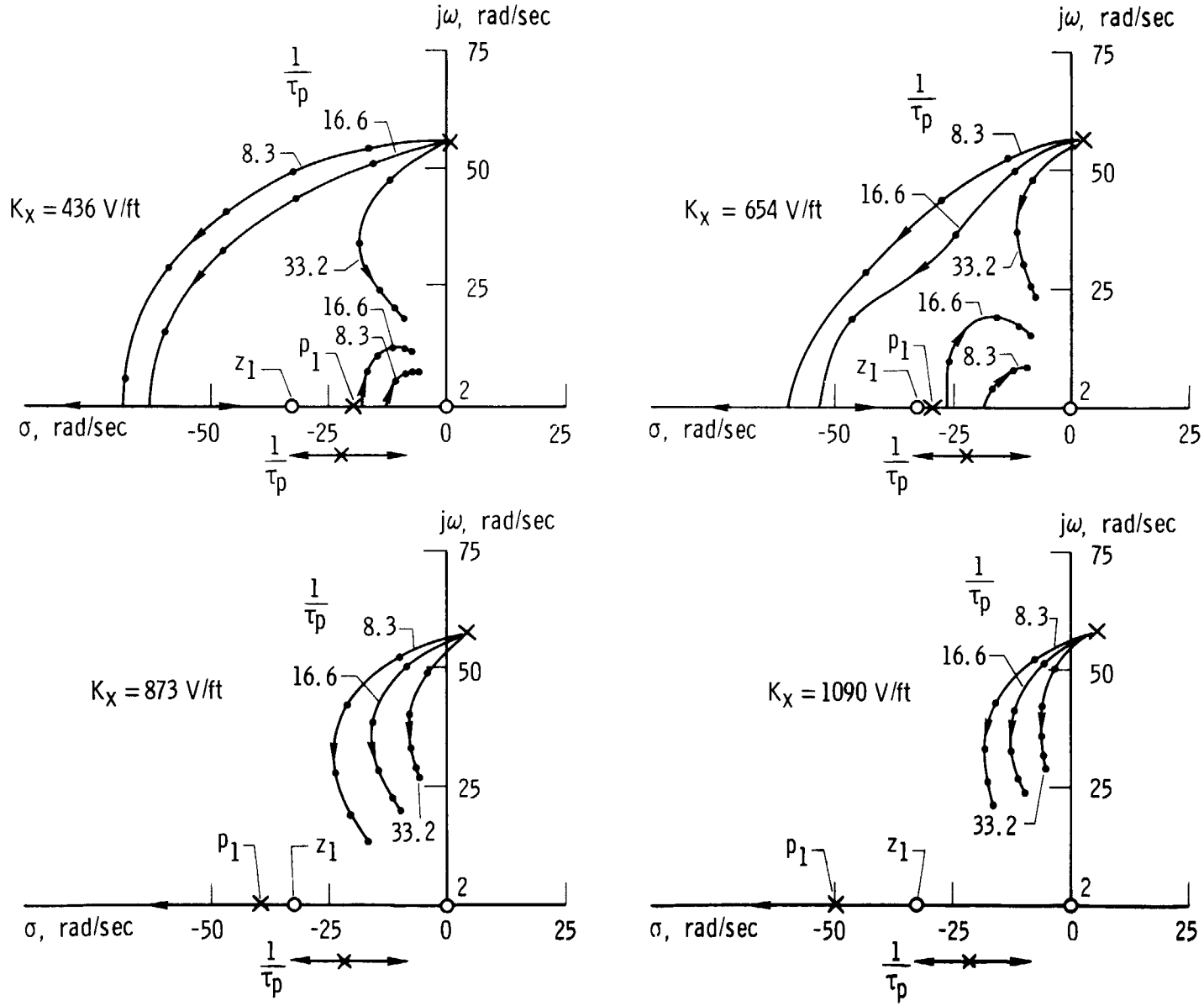

(b) Case II, $K_2 = 0$.

Figure 13. Continued.

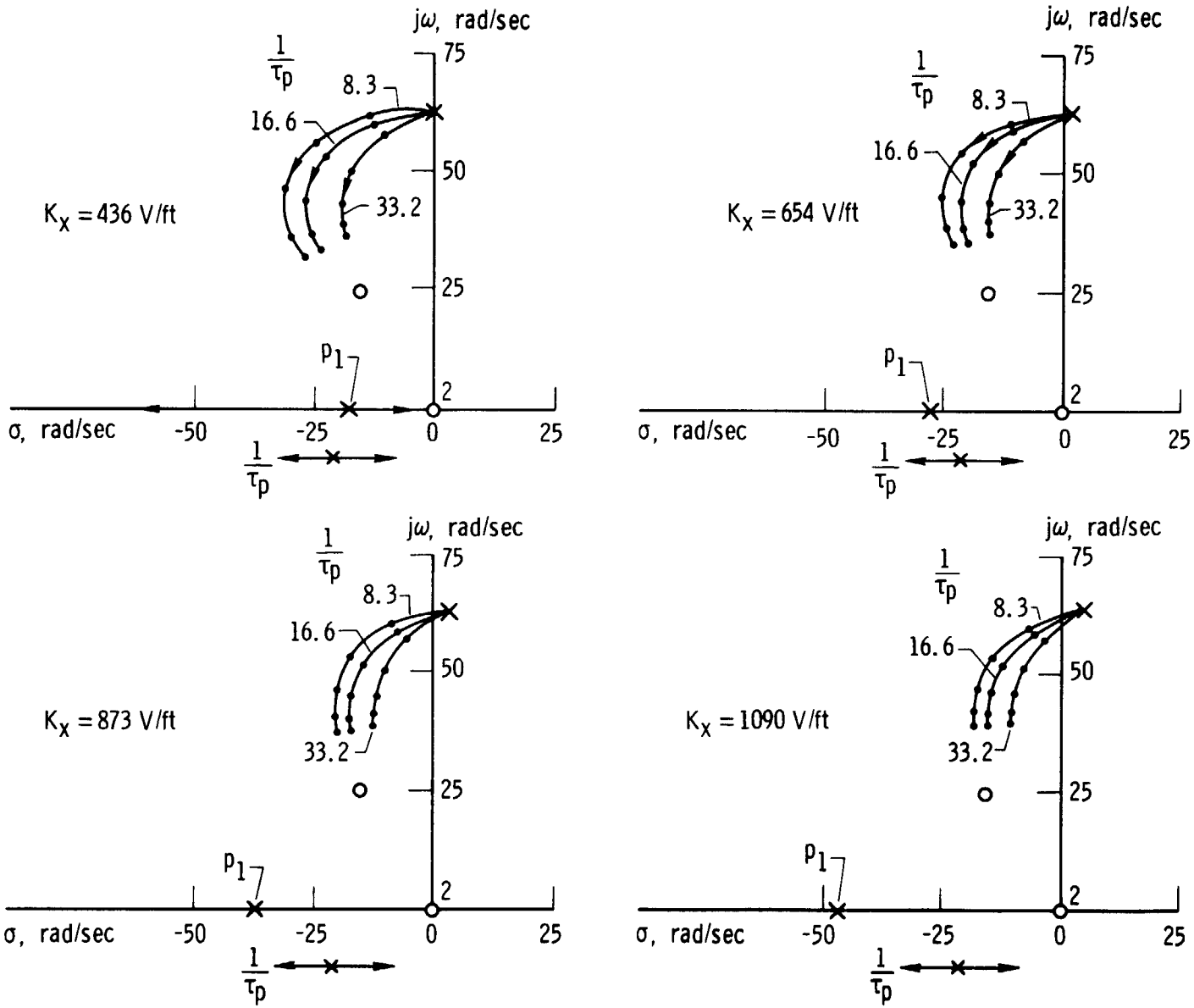

(c) Case III.

Figure 13. Concluded.

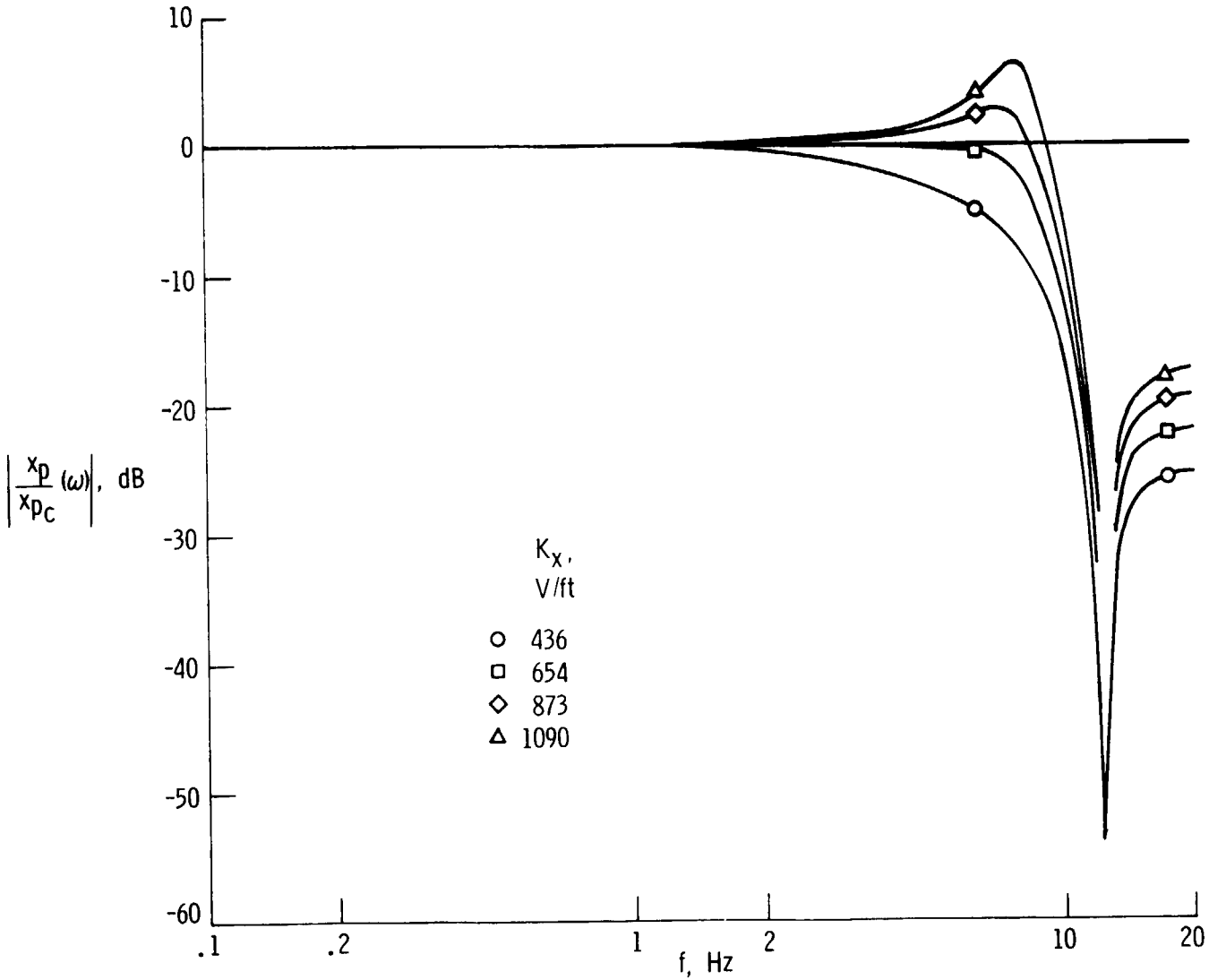

(a) Magnitude.

Figure 14. Linear model frequency response as a function of K_x. $K_p = 0.00348$ V/psi; $\frac{1}{\tau_p} = 16.6$ rad/sec.

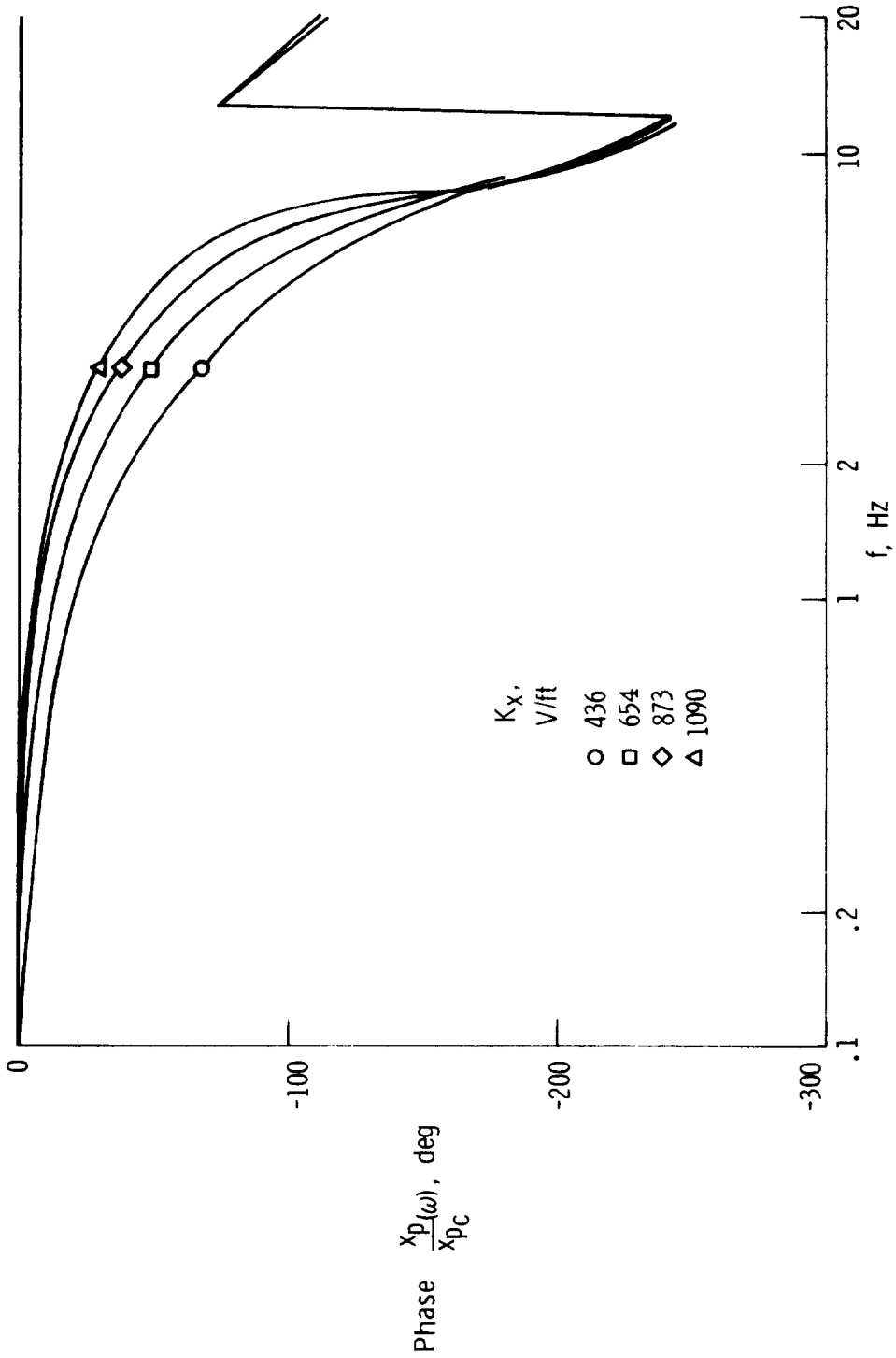

(b) Phase angle.

Figure 14. Concluded.

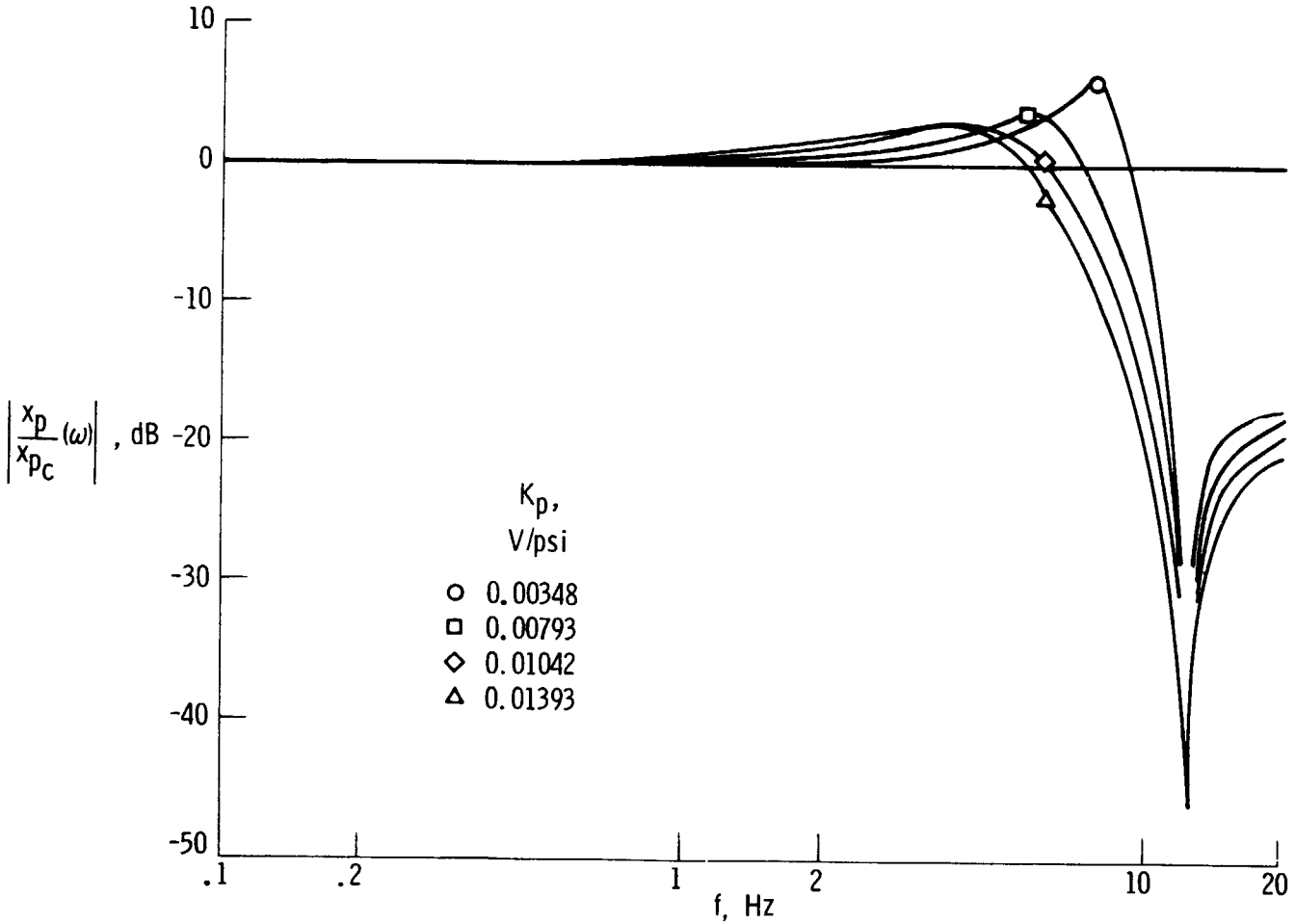

(a) Magnitude.

Figure 15. Linear model frequency response as a function of K_p. K_x = 1090 V/ft; $\frac{1}{\tau_p}$ = 16.6 rad/sec.

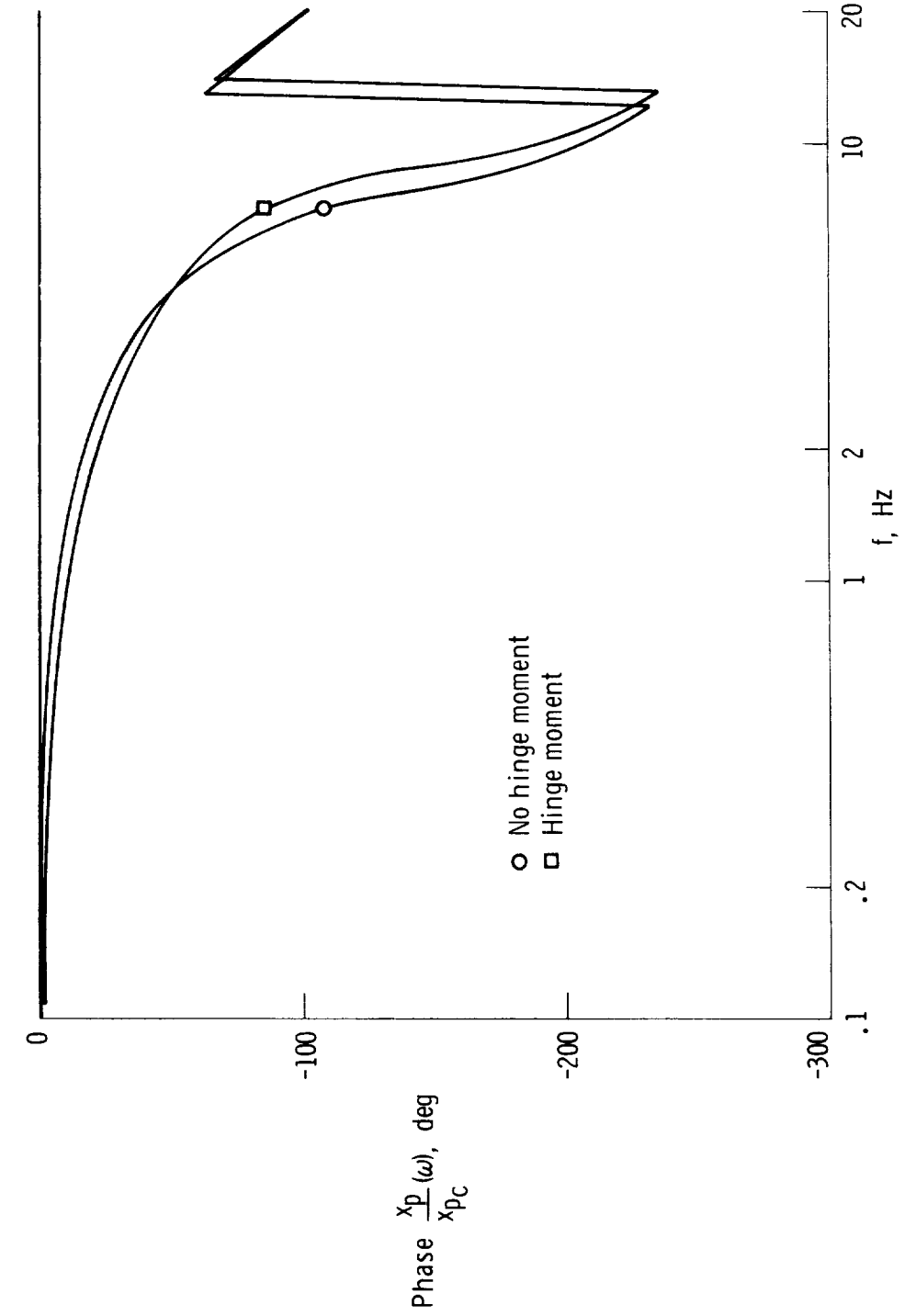

(b) Phase angle.

Figure 16. Concluded.

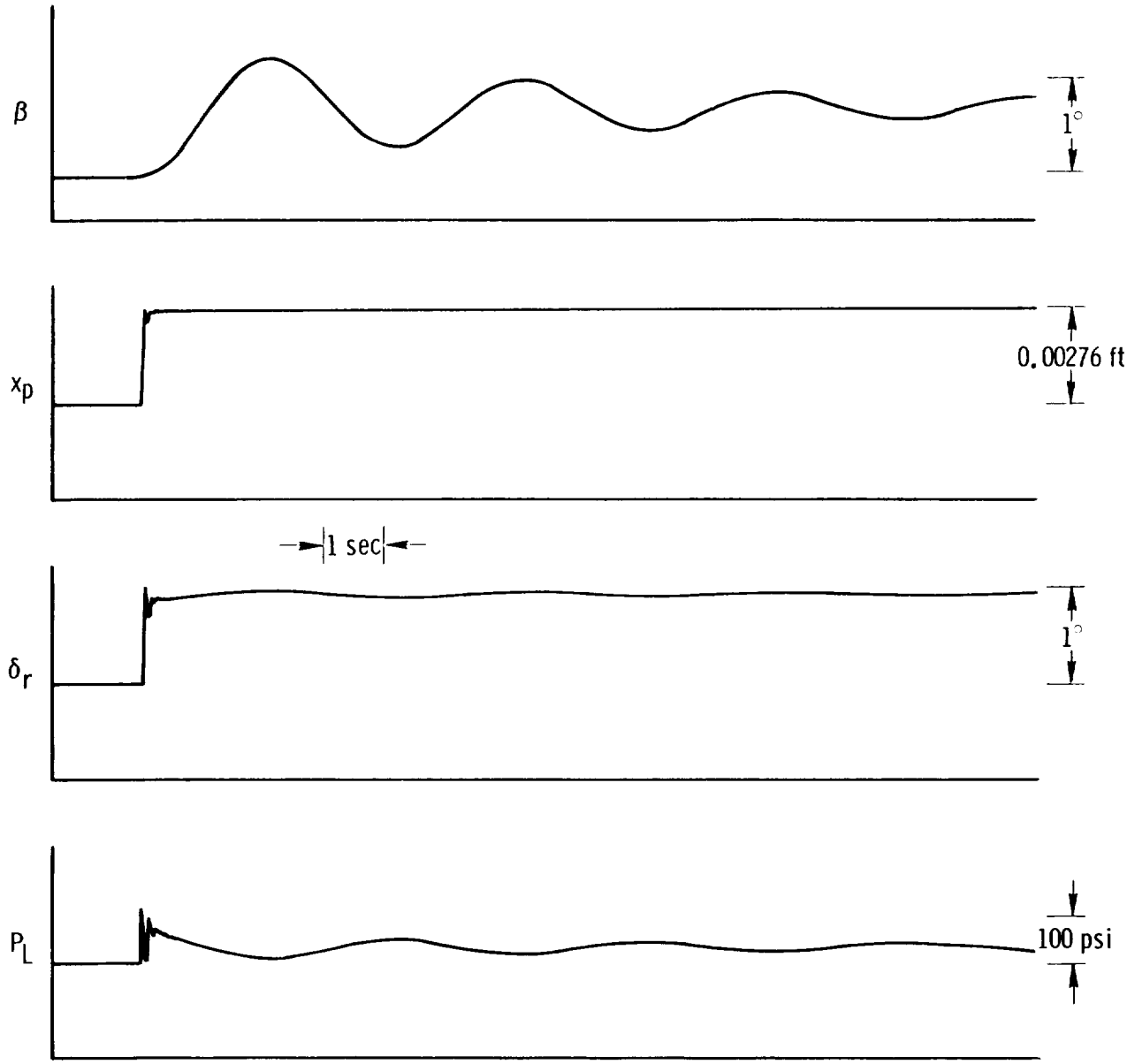

Figure 17. Hinge-moment loading of rudder surface due to β response. K_x = 1090 V/ft; K_p = 0.0048 V/psi; $\frac{1}{\tau_p}$ = 16.6 rad/sec.

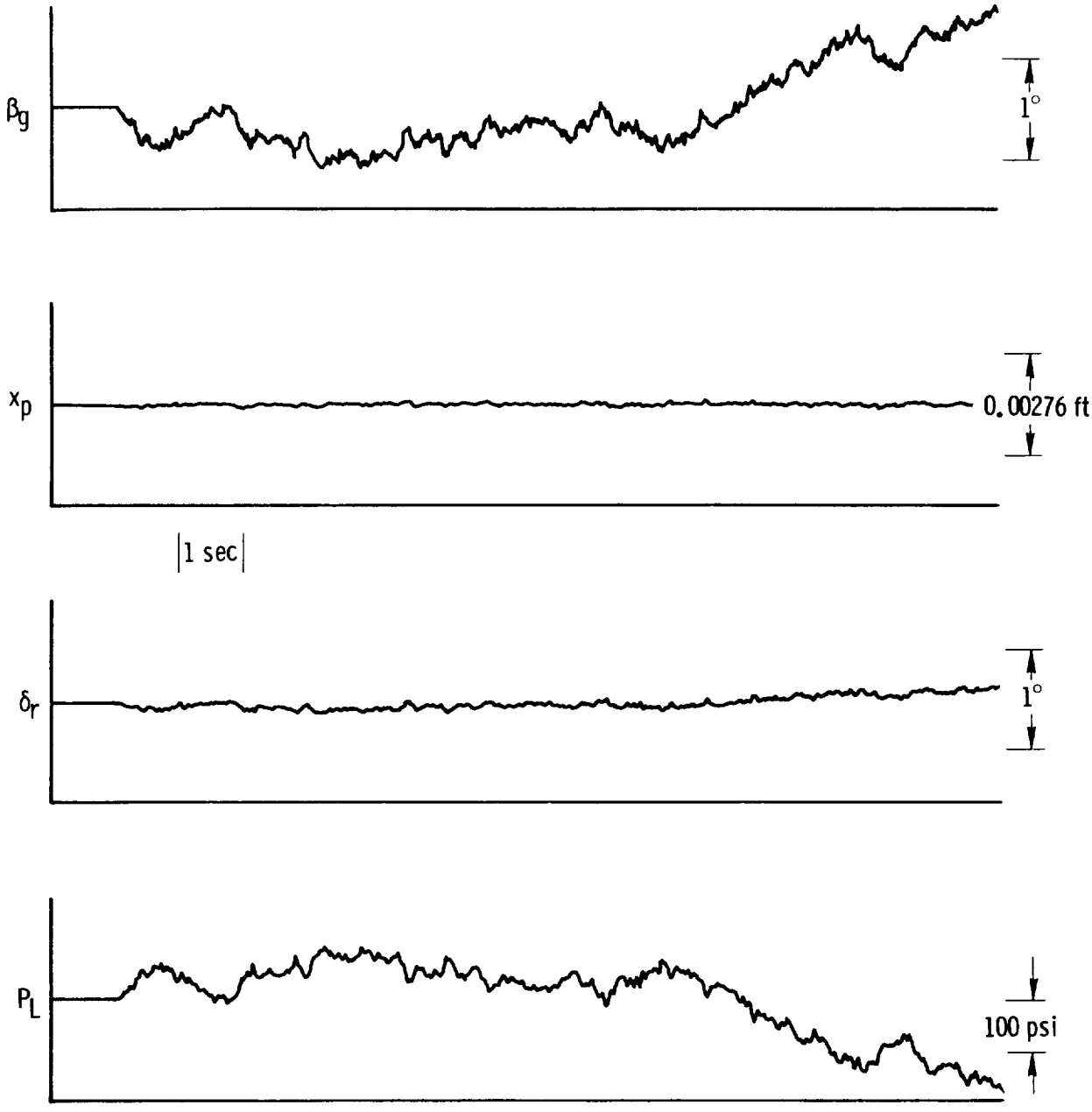

Figure 18. Response of nonlinear model to simulated atmospheric turbulence. $K_x = 1090$ V/ft; $K_p = 0.0048$ V/psi; $\frac{1}{\tau_p} = 16.6$ rad/sec; $\sigma_g = 5$ ft/sec; $\frac{L_g}{V_a} = 10$ sec.

NASA-Langley, 1972 — 2 H-629

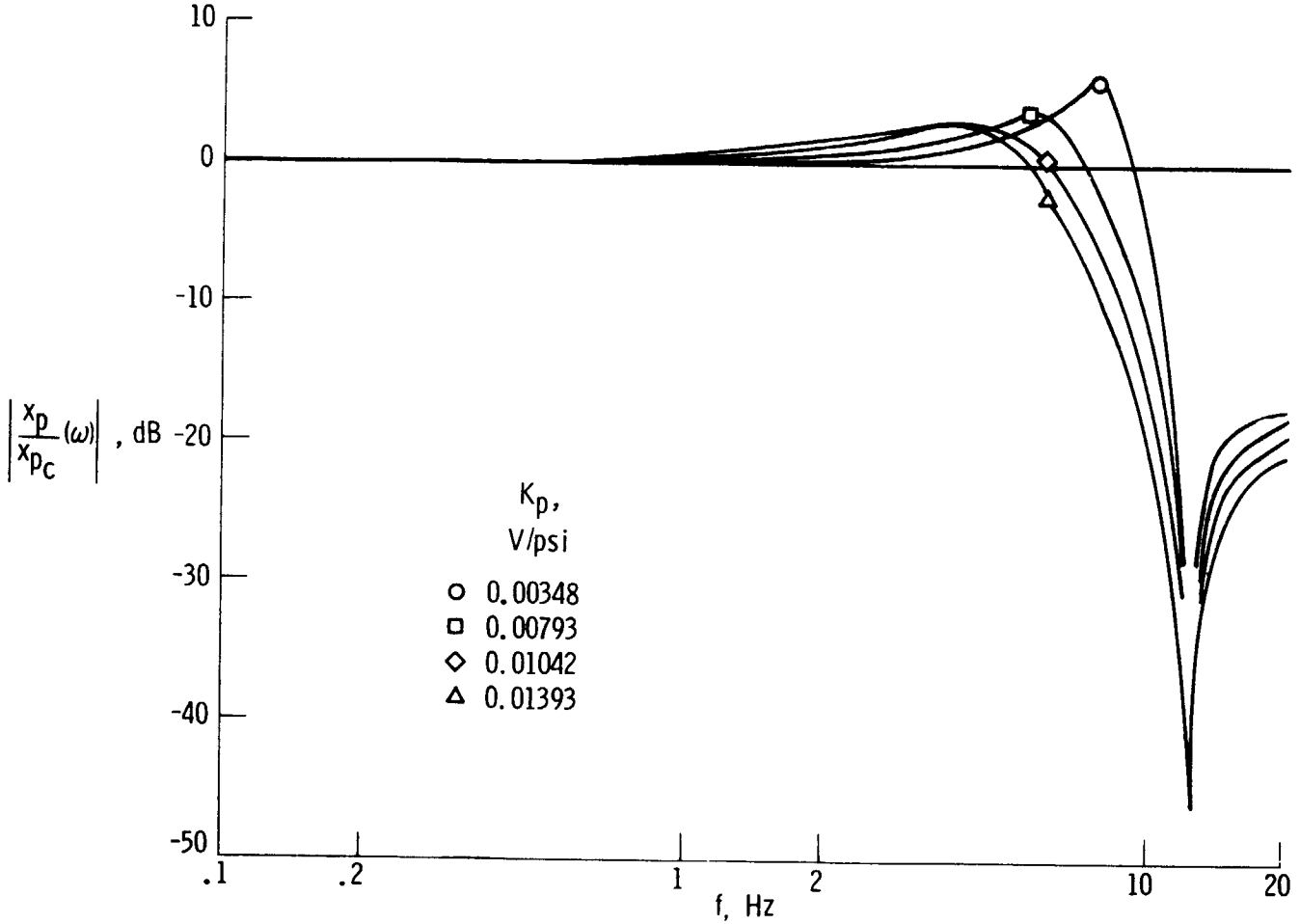

(a) Magnitude.

Figure 15. Linear model frequency response as a function of K_p. K_x = 1090 V/ft; $\frac{1}{\tau_p}$ = 16.6 rad/sec.

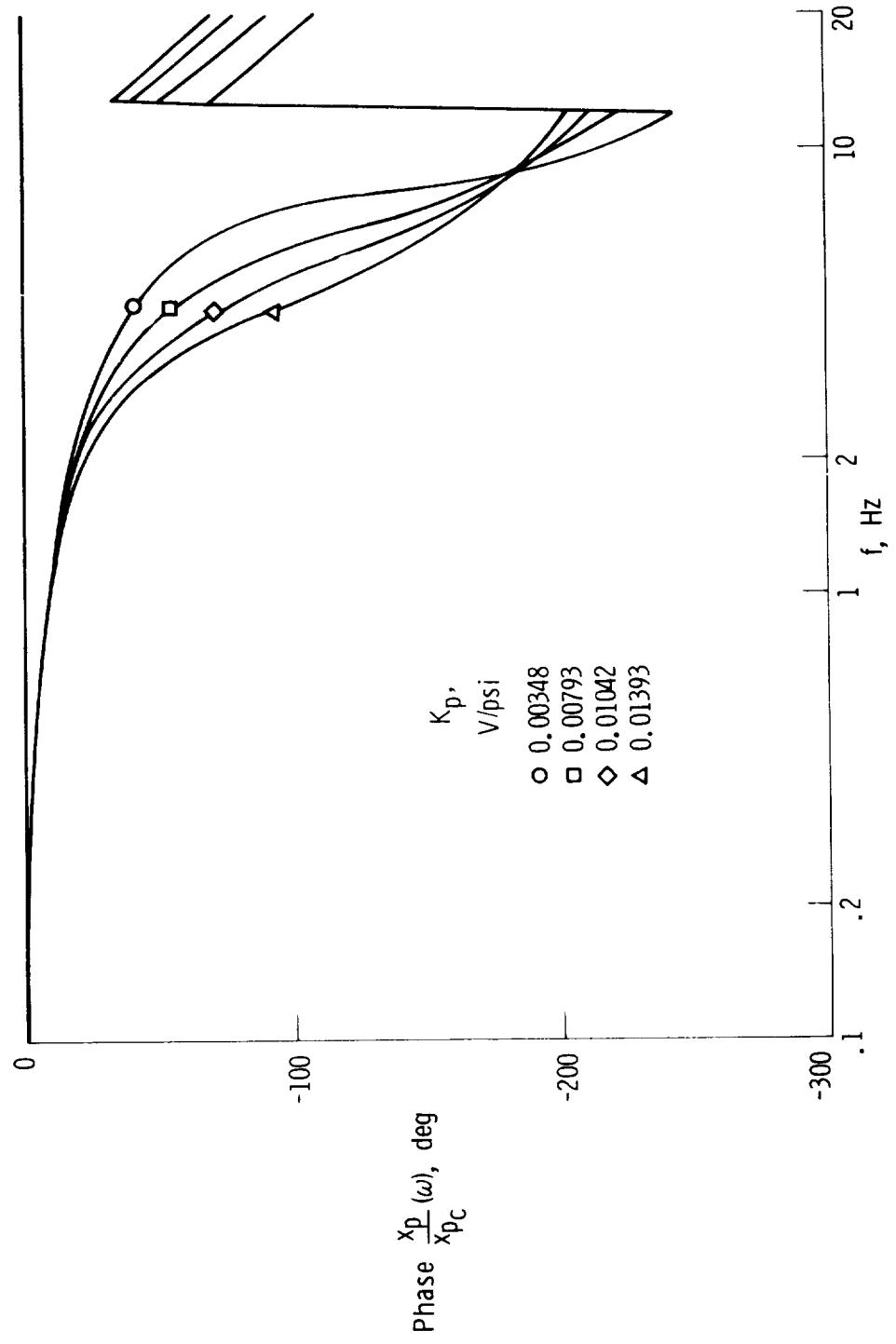

(b) Phase angle.

Figure 15. Concluded.

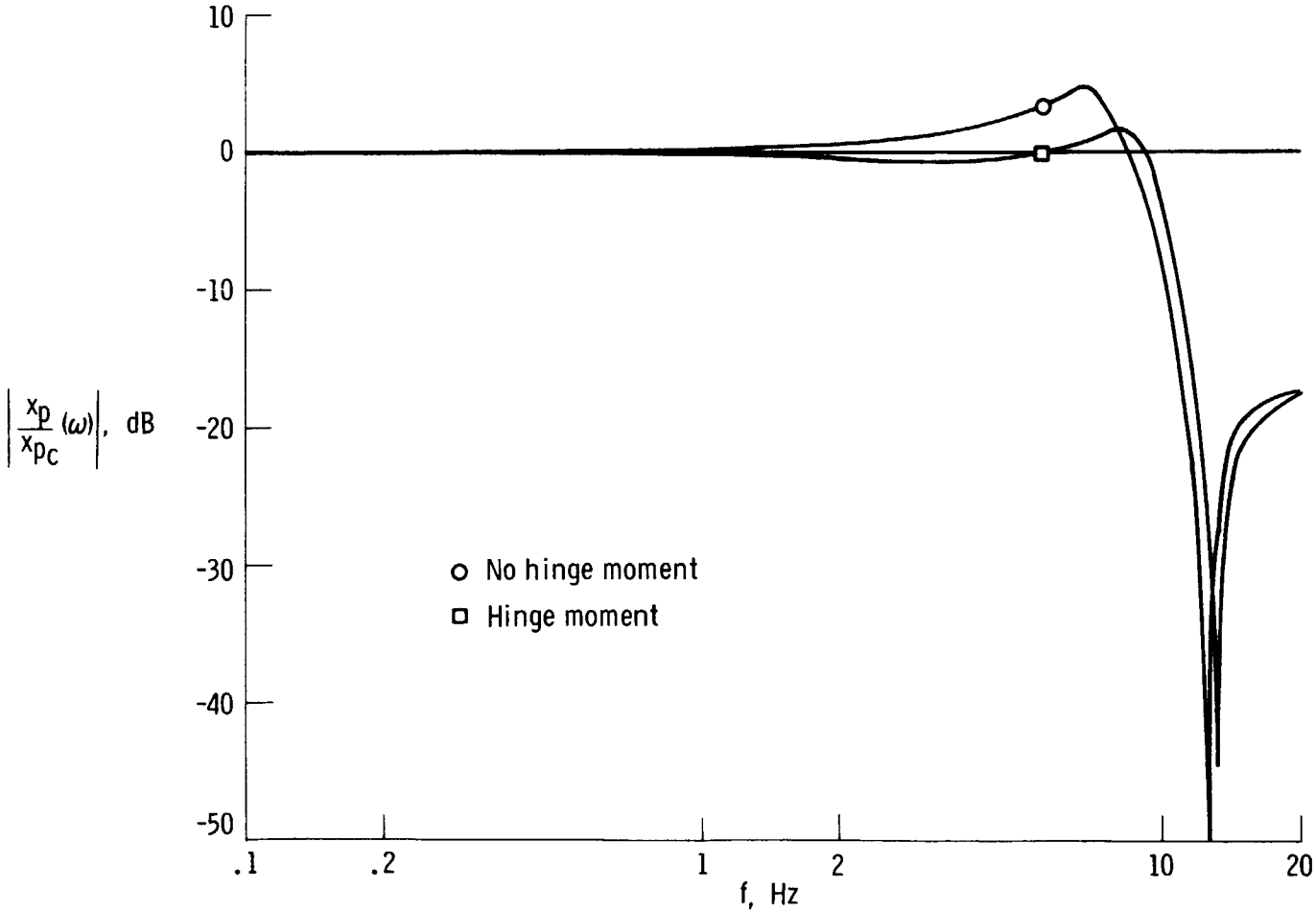

(a) Magnitude.

Figure 16. Effect of hinge-moment loading on $\frac{x_p}{x_{p_c}}$ (s) frequency response (linear model). K_x = 1090 V/ft; K_p = 0.0048 V/psi; $\frac{1}{\tau_p}$ = 16.6 rad/sec.

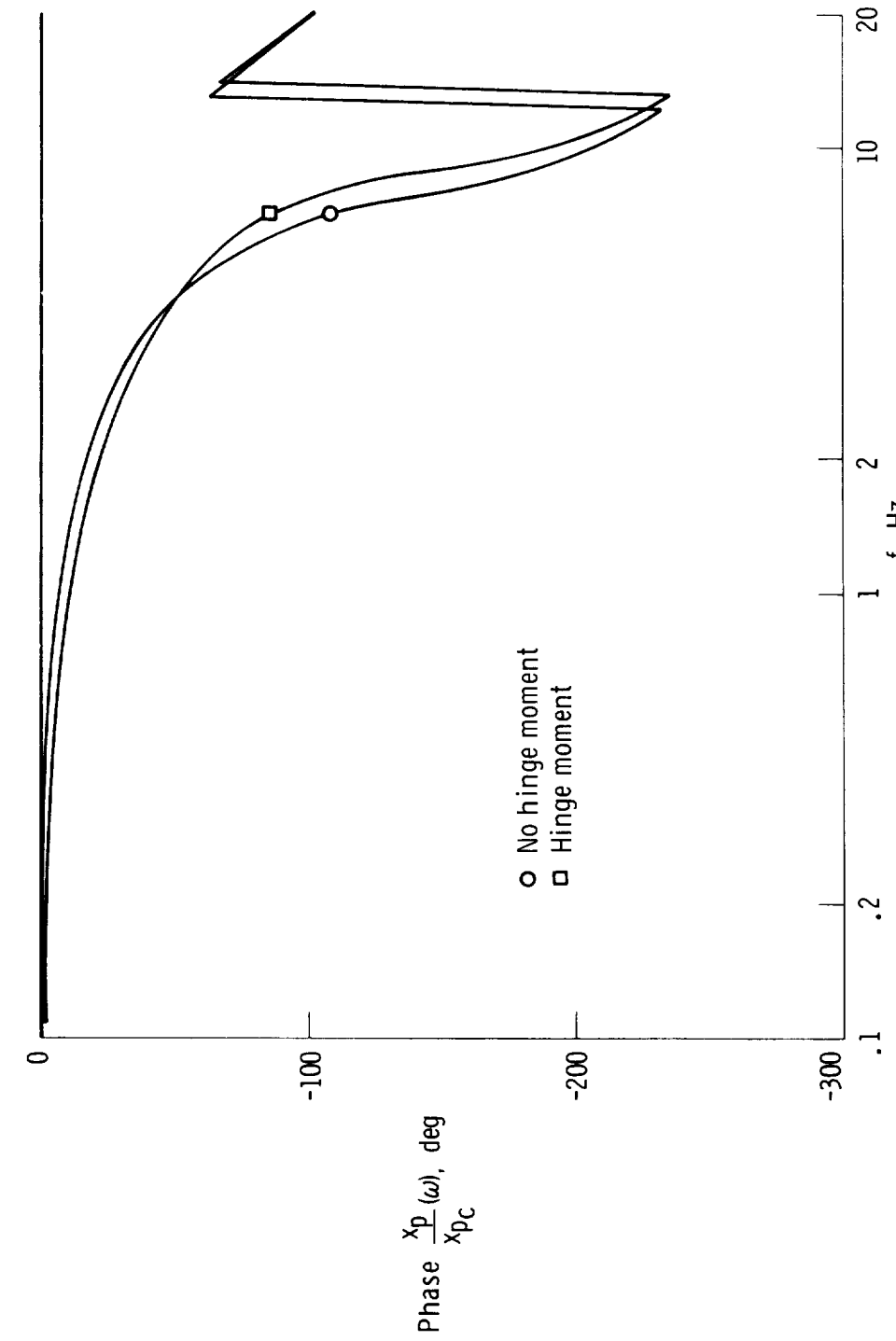

(b) Phase angle.

Figure 16. Concluded.

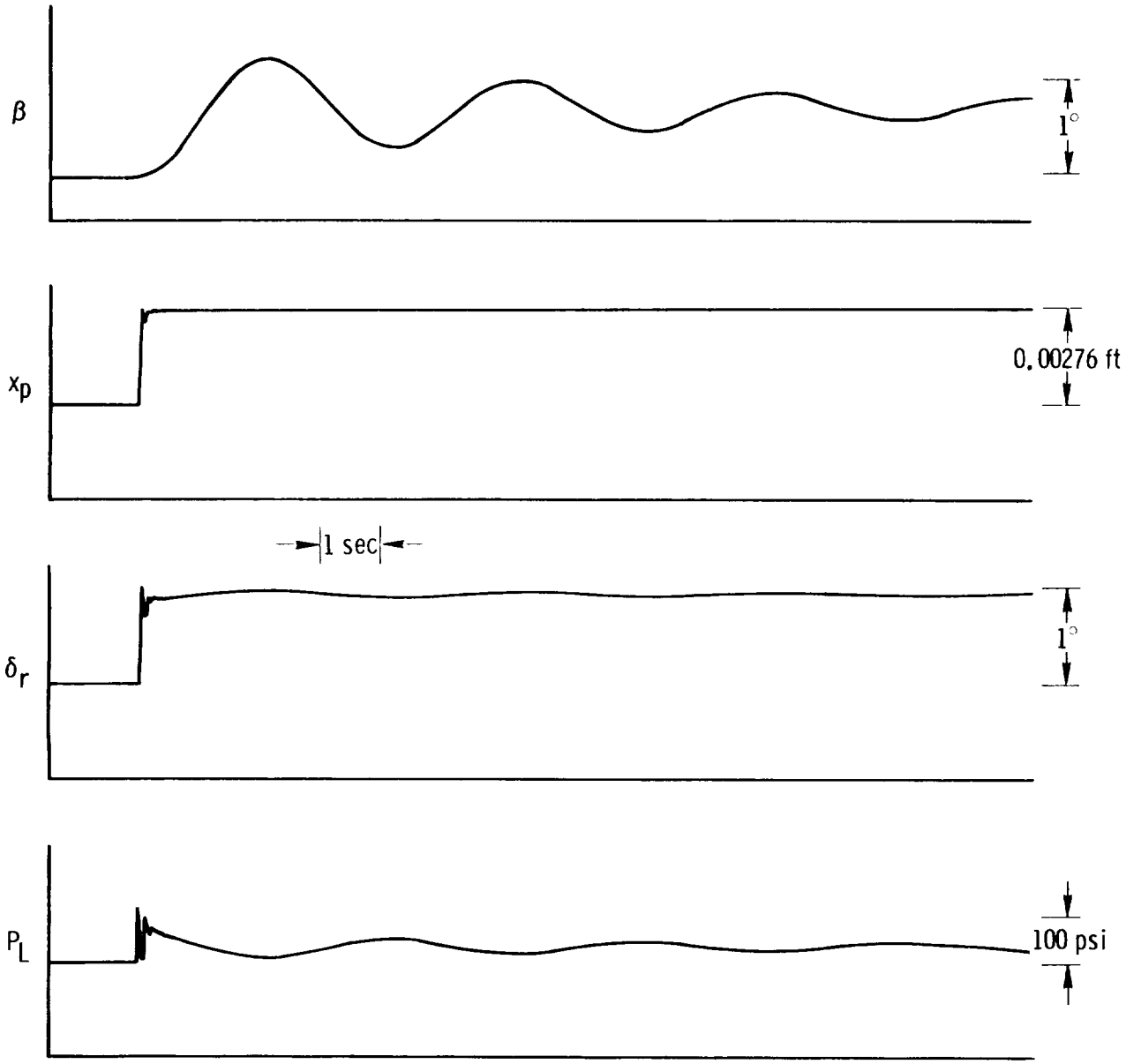

Figure 17. Hinge-moment loading of rudder surface due to β response. K_x = 1090 V/ft; K_p = 0.0048 V/psi; $\frac{1}{\tau_p}$ = 16.6 rad/sec.

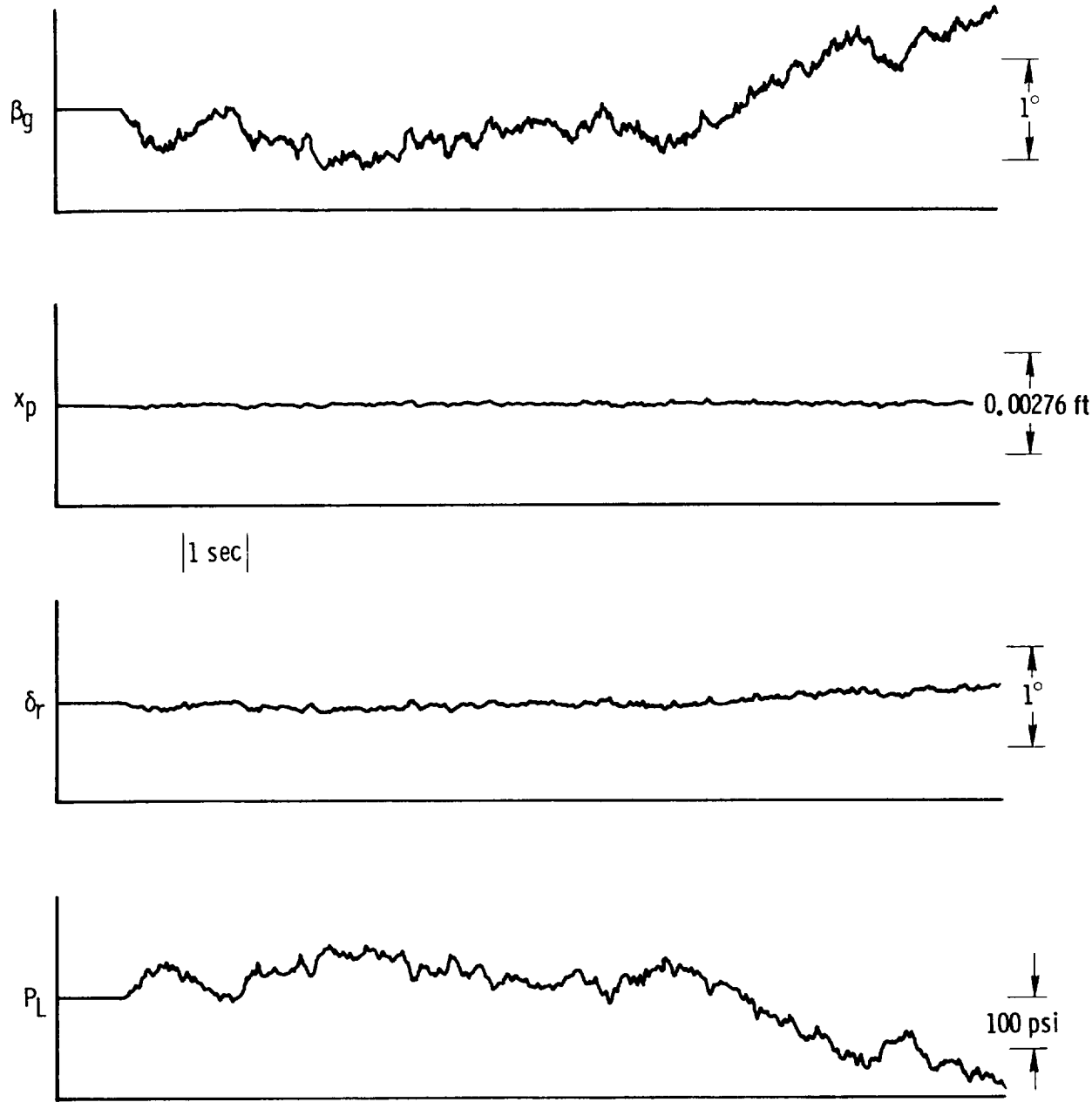

Figure 18. Response of nonlinear model to simulated atmospheric turbulence. $K_x = 1090$ V/ft; $K_p = 0.0048$ V/psi; $\frac{1}{\tau_p} = 16.6$ rad/sec; $\sigma_g = 5$ ft/sec; $\frac{L_g}{V_a} = 10$ sec.

NASA-Langley, 1972 — 2 H-629